# CORONAL JETS SIMULATED WITH THE GLOBAL ALFVÉN WAVE SOLAR MODEL

J. Szente[1], G. Toth[1], W. B. Manchester IV[1], B. van der Holst[1], E. Landi[1], T. I. Gombosi[1],
C. R. DeVore[2], and S. K. Antiochos[2]
[1] Climate and Space Sciences and Engineering Department, University of Michigan, Ann Arbor, MI 48109, USA; judithsz@umich.edu
[2] Heliophysics Science Division, NASA Goddard Space Flight Center, Greenbelt, MD 20771, USA

## ABSTRACT

This paper describes a numerical modeling study of coronal jets to understand their effects on the global corona and their contribution to the solar wind. We implement jets into a well-established three-dimensional, two-temperature magnetohydrodynamic (MHD) solar corona model employing Alfvén-wave dissipation to produce a realistic solar-wind background. The jets are produced by positioning a compact magnetic dipole under the solar surface and rotating the boundary plasma around the dipole's magnetic axis. The moving plasma drags the magnetic field lines along with it, ultimately leading to a reconnection-driven jet similar to that described by Pariat et al. We compare line-of-sight synthetic images to multiple jet observations at EUV and X-ray bands, and find very close matches in terms of physical structure, dynamics, and emission. Key contributors to this agreement are the greatly enhanced plasma density and temperature in our jets compared to previous models. These enhancements arise from the comprehensive thermodynamic model that we use and, also, our inclusion of a dense chromosphere at the base of our jet-generating regions. We further find that the large-scale corona is affected significantly by the outwardly propagating torsional Alfvén waves generated by our polar jet, across $40°$ in latitude and out to 24 $R_\odot$. We estimate that polar jets contribute only a few percent to the steady-state solar-wind energy outflow.

Key words: magnetohydrodynamics (MHD) – solar wind – Sun: corona – Sun: waves

## 1. INTRODUCTION

Jets are ubiquitous and are seen in X-ray followed by emission in cooler EUV bands, as observed with multiple instruments on board *Yohkoh*, the *Solar and Heliospheric Observatory* (*SOHO*), the *Transition Region and Coronal Explorer* (*TRACE*), *Hinode*, the *Solar Terrestrial Relations Observatory* (*STEREO*), and the *Solar Dynamics Observatory* (*SDO*). Their typical sizes range from $10^2$ to $10^4$ km, outflow speeds from $10^1$ to $10^3$ km s$^{-1}$, and lifetimes from $10^{-1}$ to $10^1$ hr (Shimojo et al. 1996; Savcheva et al. 2007; Shibata et al. 2007). They have been observed at multiple wavelength bands —visible (Bohlin et al. 1975), EUV, and X-ray (Shibata 1982) —corresponding to electron temperatures ranging from about $10^4$ to $10^7$ K. Jets are similar to spicules in size; both also contribute to the quiet corona. Although spicules contribute through slow plasma outflow at about the ion acoustic speed, jets exhibit eruptive plasma injections with fast plasma outflow at about the Alfvén speed over longer periods of time. This paper focuses exclusively on jets, which are distinct from spicules. The constant presence of jets raises the question of their contribution to the solar wind plasma and coronal heating. First, hydrodynamic (Shibata 1982), and later magnetohydrodynamic, models complemented the increasingly detailed solar disk and in situ observations and have informed us of the fine structure of jets, which also raises questions about observable traces they leave in the outer coronal plasma. Many models have attempted to reproduce and quantitatively predict jet properties to estimate their contribution to coronal heating and the solar wind, and identify their observable signatures in the extended solar atmosphere. However, even the most advanced models (3D MHD models for instance; see Section 2) studied jets without considering the background solar wind plasma interaction with the jet. Modeling the jet in a complete solar

corona instead of a local box allows the jet contribution to the global solar wind to be estimated.

In this paper, we address these two limitations and discuss two 3D MHD jet simulations realized within the Alfvén Wave Solar Model (AWSoM), which provides realistic atmospheric stratification, solar wind acceleration, and turbulence-based coronal heating (Sokolov et al. 2013; van der Holst et al. 2014). We use our simulation results to give quantitative estimates of the significance of jets' contributions to the global solar corona and to suggest observables that can be investigated with the upcoming *Solar Probe Plus* mission.

The structure of this paper is the following. After a short review of jet properties in Section 2, Section 3 describes the simulation model and Section 4 presents the results. We compare synthetic line-of-sight images to observations in Section 5 as model validation. Finally, our findings are summarized in Section 6.

## 2. JET OBSERVATIONS AND MODELS

Energy deposition in the chromospheric plasma results in various types of jets, depending on the vertical location of the process (Sterling et al. 1994). The first models of jets were hydrodynamic ones; Shibata (1982) classified jets into two categories based on the location of their bright points: the "crest-shock-"type jets have bright points at the low corona's low density plasma and are driven by shock waves. These jets can be observed in the EUV bands. The second type is the "shock-tube" jet, whose bright point is at the middle-upper chromosphere, and its driver is a large pressure gradient. Only this jet type is visible in both Hα lines (due to its higher density) and the accompanying X-ray flares. Using more detailed observations from *Yohkoh*'s Soft X-ray Telescope (SXT), jets were distinguished by the plasma temperature at which they have been observed. With SXT, Shibata et al.

(1994) observed various jets at active regions, emerging flux regions, and at X-ray bright points of their flaring footpoints. To distinguish between superhot (up to about $10^7$ K) and hot (about $10^6$ K) plasma ejections, the terms coronal X-ray and EUV jets were introduced. Jets were also related to magnetic field topology changes. Studying EUV jets, Moschou et al. (2013) found that in many cases the ejected material falls back due to its low velocity. They also reported untwisting magnetic flux and recurrence of ejections in multiple cases. Shibata et al. (1992) showed that magnetic reconnection is the driver of jets. With an increasing focus on X-ray jets, several studies have also suggested that jets are driven by magnetic reconnection events, either through spectroscopic observations (Kim et al. 2007) or multi-spacecraft observations (Madjarska 2011). Jet formation by reconnection between twisted and untwisted magnetic loops in open- and closed-field regions has been observed by SXT. Moreover, rotating motions, spinning and unwinding, and magnetic flux cancellation were observed in multiple bands: Ca II H and EUV with *Hinode*'s instruments (Solar Optical Telescope (SOT), X-ray Telescope (XRT), EUV imaging spectrometer (EIS)), with the Extreme Ultraviolet Imager (EUVI) on board *STEREO* (Sterling et al. 2010), or with the Atmospheric Imaging Assembly (AIA) on board *SDO* (Chen et al. 2012). In a study of nine jets using observations from SXT and the Mees CCD Imaging Spectrograph and Imaging Vector Magnetograph at the Mees Solar Observatory, Canfield et al. (1996) found that X-ray jets and Hα surges are associated with moving magnetic bipoles. They reported spinning motion in all observed surges, consistent with the untwisting of the magnetic field. They also discussed the morphology of jets, including the up- and downflow of reconnection exhaust. Evidence of helical structures within jets has been confirmed with stereoscopic observations by the *STEREO* spacecraft (Patsourakos et al. 2008). Overall, both EUV and X-ray jets are suggested to be produced by small-scale reconnection events (Chifor et al. 2008b). These multiple wavelength observations showed not only the recurrent reconnection, but also the mixing of dense, cold plasma with tenuous, hot plasma. They also showed that within the jet plasma, the density increased with increasing upflow velocity.

Being closely tied to magnetic field evolution, another common classification of X-ray jets is based on the relative direction of the coronal field the flux emerges into: in the cases of nearly horizontal fields, the jet is a "two-sided loop" type, while the ones emerging into vertical or moderately tilted fields are "anemone" jets (Shibata et al. 1994). Shimojo et al. (1996) suggested that the anemone morphology is due to the emergence of a bipole magnetic structure into the open flux, based on a statistical study of a hundred X-ray jets. The different jet types seemed to relate to each other in morphology and based on their driving forces. Shibata et al. (2007) observed 59 jets with Ca II H broadband filters, which were called "Ca jets." They estimated that during the one-hour SOT observation, the jet did not provide sufficient energy flux to heat the ambient corona. The inferred magnetic structures of these anemone-shaped jets were assumed to be due to an opposite-polarity magnetic dome being reconnected with the ambient open field. The drivers of these jets were the reconnecting fields at the footpoints of the dome. A similar driving mechanism was suggested in jet models of different sizes and vertical locations: coronal X-ray jets are the largest, followed by EUV jets, and then photospheric nanoflares. As Nishizuka et al. (2011) pointed out, the chromospheric and coronal anemone jets show very similar dynamics.

Jets are often observed with accompanying bright spots in the local plasma. The appearance and reappearance of bright points along with jets were studied from multiple aspects. Kamio et al. (2007) and Pucci et al. (2012) showed that jets and bright points are strongly correlated and concluded that jets are the result of magnetic topology change—reconnection events. Kamio also found evidence of up- and downflows, which are evidence of reconnection outflow. Coronal hole bright points and a particular jet were studied using EIS observations by Doschek et al. (2010). They found a Doppler shift in the Fe XII line toward the observer, and the jet speed was measured to be about 15–20 km s$^{-1}$. The speed decreased to zero toward the base, which was also the hottest part of the jet. The maximum observed temperature was about $1.4 \times 10^6$ K and decreased with height, which suggested that heating occurred at the base of the jet. Expanding bright loop structures prior to the jet onset were observed by Singh et al. (2012). Here, chromospheric anemone jets showed intermittent and recurrent ejections, and some also showed signs of current-sheet formation or quasi-periodicity. Shimojo et al. (2007) discussed that jets along closed magnetic field lines might cause brightening at the other end of the loop structure like a reverse jet. Using observations of smaller loops, they were able to measure the speed of the hot plasma flow along the loop structure that causes the brightening at the other footpoint. In addition, they remarked on the fine structures of X-ray jets in the XRT observations: the majority of observed jets appeared after a brightening which was followed by a loop expansion, possibly due to kinking. A statistical study of 100 jets observed during a six-month period in 1991–1992 with SXT by Shimojo et al. (1996) showed that the majority of jets included footpoint brightening: 27% of the bright regions were clearly above the actual footpoints, which suggested that the reconnection and localized plasma heating take place around the dome.

Having multiple detailed observations with instruments aboard *Hinode* and *SDO*, the jet categorization moved forward: Moore et al. (2010, 2013) set up a classification based on morphology, phase, and magnetic reconnection scenario. They concluded that there are two basic types of X-ray jets: standard and blowout jets. They occur approximately in equal numbers, but standard jets are dimmer, and so they are more likely to be missed during observations. Blowout jets show lateral expansion of cool material, standard jets do not. Also, blowout jets have a more complex structure and are accompanied by stronger brightenings than standard jets. Standard jets consist of one spire, usually having the shape of an inverted Y, without any strong X-ray brightening or lateral expansion.

Pucci et al. (2013) further analyzed in detail the differences (velocity, temperature, magnetic field strength) and similarities (recurrent reconnection events) between standard and blowout jets. Both types show axial rotation and are produced by bipolar magnetic fields emerging into the ambient field. Also, an observational study by Adams et al. (2014) proved that blowout jets can occur with flux convergence rather than emergence, and that a jet structure can be produced by destabilization along the polarity inversion line. This blowout eruption is like a filament eruption similar to CMEs and flares. The reconnection between the blowing-out arcade field constructs long EUV loops, which are identified as new types of blowout jets.

Due to the nature of line-of-sight observations many non-jet events may produce jet-like features in the field of view. Madjarska et al. (2007) showed that jet-like features may be produced by fast field-aligned flows, but by using spectroscopic tools it is possible to clearly describe the ongoing dynamics and distinguish such flows from jet events. Similarly, apparently helical, twisting structures in prominences were observed by Okamoto et al. (2010) and Li et al. (2012) to be in the form of jets. In many cases, the apparent twist was created by overlapping field lines with loop-like geometries (Panasenco et al. 2014).

Another open question is the estimation of jet contribution to the solar wind plasma. Wang et al. (1998) suggested that jets occurred more often than observed, and that it is not clear how to estimate their significance. Similarly, observations of jets from *SOHO*'s Large Angle Spectrometric COronagraph (LASCO) C2 were analyzed by Corti et al. (2007) to find correlating *Ulysses* plasma measurements. Due to the very active corona, it was not easy to correlate the disturbances caused by the jet to *Ulysses* observations. They found that cold jets, initiated by reconnection of closed loops with the open background field, preserved the temperature signatures during propagation, and that the ejected mass is above $10^{11}$ g, which means that these jets should be observable by available coronagraphs, such as LASCO.

Numerical models have been used to study the morphology and quantitatively estimate the properties of jets for decades. Recently Cranmer & Woolsey (2015) have shown in the context of a reduced MHD simulation that Alfvénic turbulence within an expanding, circular flux tube can cause signatures in the coronal plasma that correspond to Type II spicules or network-jets observed by IRIS. In their model, chromospheric Alfvén waves develop into compressive waves that produce the shocks, driving the dense plasma from the chromospheric and transition regions to heights of thousands of kilometers in the corona. With a 1D hydrodynamic study, Sterling et al. (1993) discussed the many possible outcomes of energy deposition, depending on the rate and vertical height, and gave descriptions of the drivers of the emerging plasma ejections. They also predicted the bands where to look for observable brightening corresponding to the location of deposition. Using 2D resistive MHD models with a uniform gravitational field, Yokoyama & Shibata (1995) showed that cool Hα surges and hot X-ray jets can both originate from microflares (see also Yokoyama & Shibata 1996). They also found that all physical and morphological characteristics were reproducible for both two-sided loop and anemone types of jets. In their model, fast-mode shocks were produced at the reconnection site with the ambient field, which drove the jet further. Later, also with a 2D resistive MHD model with a uniform gravitational field, Nishizuka et al. (2008) successfully reproduced anemone jet features observed by SOT, XRT, and by *TRACE* at 195 Å. Using a 2.5D resistive MHD model with a uniform gravitational field, Yokoyama & Shibata (1999) estimated that only 3% of energy was stored as waves generated in the jet during the reconnection. In another 2.5D MHD study, Yang et al. (2013) showed that moving magnetic features can create chromospheric anemone jets, along with tearing instabilities and slow-mode shocks in them.

Using a fully 3D approach to flux emergence within an open-field region, Moreno-Insertis & Galsgaard (2013) produced blowout jets with a stratified background atmosphere starting with a twisted flux rope below the photosphere. The model used ideal gas and uniform heating approximations. They successfully reproduced the standard and blowout phases of a jet, as described by Moore et al. (2010, 2013, 2015). In a related study, the Block Adaptive Tree Solar-wind Roe-type Upwind Scheme (BATS-R-US) (Powell et al. 1999; Tóth et al. 2012) was used for modeling jet formation by Fang et al. (2014) in a fully 3D ideal MHD setup. They simulated the emergence of a twisted flux rope into the ambient open field, and found that the coronal mass is increased by about 2% due to the mass injection through the jet. The generated upward flow was strongly dominated by the magnetic twist, while the downflow was simpler, but still correlated with the magnetic twist. They concluded that the upward motion was accelerated strongly by the Lorentz force, and that the Poynting flux in the corona was dominated by the twisting motion that coincided with the upward mass transport of dense plasma. The field-aligned thermal conduction also transported energy downward to the lower atmospheric regions, inducing further plasma release by evaporation.

An alternative mechanism for generating coronal jets was proposed on theoretical grounds by Antiochos (1990, 1996). He argued that the null-point "anemone" topology of the source region would be susceptible to explosive magnetic reconnection that could drive the jet, even in regions where no new flux is emerging. This model has been investigated in a series of numerical simulations by Pariat et al. (2009, 2010, 2015) and Karpen et al. (2016). In these studies, the closed magnetic flux of the jet source region is energized by slow footpoint motions that introduce twist and cause the volume of closed flux to become distended along the ambient open field. Eventually, the flux succumbs to an ideal kinking or toppling instability, which ruptures the separatrix surface and drives fast reconnection between the internal, twisted closed flux and the external, untwisted open flux. The transfer of twist to the external field initiates nonlinear Alfvén waves on the reconnected open field lines, which are trailed by outflows of dense plasma that constitute the jet. This mechanism has been shown to produce recurrent jets in response to continued slow footpoint driving (Pariat et al. 2010) and to spawn jets that propagate into the outer corona when solar gravity, wind, and spherical expansion are taken into account (Karpen et al. 2016). However, these previous simulations assumed either adiabatic or isothermal evolution of the plasma, which is not adequate for predicting the density and temperature signatures of coronal jets observed on the Sun.

The objective of our paper is to remedy this omission by using a two-temperature model of the global corona that includes the complexities of heat conduction, optically thin radiative losses, and background atmospheric heating due to Alfvén waves. This far more comprehensive model of the coronal thermodynamics is described in Section 3. We employ it to simulate the generation of coronal jets driven by slow footpoint motions at the chromosphere, in a manner analogous to that of Pariat et al. (2009), as detailed in Section 4.

## 3. SIMULATION DESCRIPTION

### 3.1. Coronal Model

The computational model is based on the BATS-R-US code that is used as the Solar Corona component of the Space Weather Modeling Framework developed at the University of Michigan (Tóth et al. 2012). We use the fully self-consistent, two-temperature (electrons and protons) AWSoM (van der

Holst et al. 2014) implemented in BATS-R-US. In this model, the corona and solar wind are heated by low-frequency Alfvén-wave turbulence, and the Alfvén-wave pressure is the main driver of the fast solar wind outflow. The governing equations of our AWSoM model are the following:

$$\frac{\partial \rho}{\partial t} + \nabla \cdot (\rho \boldsymbol{u}) = 0, \tag{1}$$

$$\frac{\partial (\rho \boldsymbol{u})}{\partial t} + \nabla \cdot \left( \rho \boldsymbol{u}\boldsymbol{u} - \frac{\boldsymbol{B}\boldsymbol{B}}{\mu_0} \right) + \nabla \left( P_p + P_e + \frac{B^2}{2\mu_0} + P_A \right)$$
$$= -\rho \frac{GM_\odot}{r^3} \boldsymbol{r}, \tag{2}$$

$$\frac{\partial \boldsymbol{B}}{\partial t} - \nabla \times (\boldsymbol{u} \times \boldsymbol{B}) = 0, \tag{3}$$

$$\frac{\partial}{\partial t} \left( \frac{P_p}{\gamma - 1} + \frac{\rho u^2}{2} + \frac{B^2}{2\mu_0} \right) + \nabla \cdot \left[ \left( \frac{\rho u^2}{2} + \frac{\gamma P_p}{\gamma - 1} + \frac{B^2}{\mu_0} \right) \boldsymbol{u} \right.$$
$$\left. - \frac{\boldsymbol{B}(\boldsymbol{u} \cdot \boldsymbol{B})}{\mu_0} \right] = -(\boldsymbol{u} \cdot \nabla)(P_e + P_A)$$
$$+ \frac{N_p k_B}{\tau_{ep}} (T_e - T_p) + Q_p - \rho \frac{GM_\odot}{r^3} \boldsymbol{r} \cdot \boldsymbol{u}, \tag{4}$$

$$\frac{\partial}{\partial t} \left( \frac{P_e}{\gamma - 1} \right) + \nabla \cdot \left( \frac{P_e}{\gamma - 1} \boldsymbol{u} \right) + P_e \nabla \cdot \boldsymbol{u}$$
$$= -\nabla \cdot \boldsymbol{q}_e + \frac{N_p k_B}{\tau_{ep}} (T_p - T_e) + Q_e - Q_{rad}, \tag{5}$$

$$\frac{\partial w_\pm}{\partial t} + \nabla \cdot [(\boldsymbol{u} \pm \boldsymbol{V}_A) w_\pm] + \frac{w_\pm}{2} (\nabla \cdot \boldsymbol{u})$$
$$= \mp \mathcal{R} \sqrt{w_- w_+} - \Gamma_\pm w_\pm. \tag{6}$$

Equation (1) is the continuity equation, where $\rho$ is the mass density and $\boldsymbol{u}$ is the proton bulk velocity. The electron velocity is assumed to be the same as the proton velocity. Equation (2) is the momentum equation in which $\boldsymbol{B}$ is the magnetic field, $\mu_0$ is the vacuum permeability, $P_{e,p}$ are the isotropic electron and proton pressures, $P_A$ is the Alfvén-wave pressure

$$P_A = (w_+ + w_-)/2 \tag{7}$$

where $w_{+,-}$ are the parallel and antiparallel (relative to $\boldsymbol{B}$) propagating Alfvén-wave energy densities, $G$ is the gravitational constant, $M_\odot$ is the solar mass, and $\boldsymbol{r}$ is the position vector originating from the solar center. We ignore solar rotation. Equation (3) is the induction equation for ideal MHD. Equation (4) is the proton pressure equation: $\gamma = \frac{5}{3}$ is the polytropic index, $N_p$ is the proton number density, $k_B$ is the Boltzmann constant, $\tau_{ep}$ is the electron/proton temperature equilibration time due to Coulomb collisions, $T_{e,p}$ are the isotropic electron and proton temperatures, and $Q_p$ is the proton heating function. We use the ideal equation of state for both electrons and protons: $P_{e,p} = N_{e,p} k_B T_{e,p}$. Equation (5) describes the evolution of electron pressure: $\boldsymbol{q}_e$ is the electron heat flux,

$$\boldsymbol{q}_e = f_S \boldsymbol{q}_{e,S} + (1 - f_S) \boldsymbol{q}_{e,H}, \tag{8}$$

where

$$f_S = \frac{1}{1 + (r/[5R_\odot])^2} \tag{9}$$

and

$$\boldsymbol{q}_{e,S} = -\kappa_e T_e^{5/2} \boldsymbol{b}\boldsymbol{b} \cdot \nabla T_e \tag{10}$$

is the Spitzer collisional heat flux and

$$\boldsymbol{q}_{e,H} = \frac{3}{2} \alpha p_e \boldsymbol{u} \tag{11}$$

is the Hollweg collisionless heat flux (Hollweg 1978) with $\alpha = 1.05$, $\boldsymbol{b} = \boldsymbol{B}/B$ is the magnetic field unit vector, and $\kappa_e = 9.2 \times 10^{-12}$ W m$^{-1}$ K$^{-7/2}$. With this description, the heat conduction is the Spitzer formulation in the dense lower corona and smoothly transitions to the collisionless regime of the upper corona at $r \approx 5R_\odot$. Additionally, $Q_e$ is the electron heating function and $Q_{rad}$ is the optically thin radiative energy loss,

$$Q_{rad} = N_e N_p \Lambda(T_e), \tag{12}$$

where $\Lambda(T_e)$ is the radiative cooling function from CHIANTI 7.1 (Landi et al. 2013). Equation (6) describes the evolution of the Alfvén-wave energy densities $w_\pm$. $\boldsymbol{V}_A = \boldsymbol{B}/\sqrt{\mu_0 \rho}$ is the Alfvén speed, $\mathcal{R}$ is the reflection rate (see details in Section 4.8), and $\Gamma_\pm$ is the dissipation rate (also discussed in Section 4.8). The + and − subscripts correspond to waves propagating parallel and antiparallel, respectively, to the local magnetic field direction. For the details of partitioning the Alfvén-wave heating between the electrons and protons ($Q_e$ and $Q_p$), see Chandran et al. (2011) or the summary presented in van der Holst et al. (2014).

We note that the equations above lack physical resistivity and viscosity, because in a global model it is not possible to resolve the scales corresponding to physical resistivity with our computational resources. The Spitzer resistivity in the chromospheric boundary plasma is of the order of $10^{-4}$ $\Omega$ m. With a time step of 0.04 s, the physical resisitivity scales are on the order of meters, which is not feasible to resolve.

Instead of physical viscosity and resistivity, the model relies on numerical viscosity and resistivity that result from the numerical diffusion terms that stabilize the solution as well as ensure that fast reconnection is possible (and occurs) in the simulation. Away from discontinuities the numerical diffusion terms are greatly reduced as the solution is spatially second-order accurate. Numerical diffusion terms have no significant effect on the solution in these smooth regions, because larger-scale structures are well-resolved on the grid, so that the diffusion timescale is long compared to the dynamic timescale. Near discontinuities, such as shock waves and current sheets, the code relies on the numerical dissipation and the conservation laws to get the right solution. For example at reconnection regions, where the current sheet steepens to a discontinuity at the level of the local grid resolution, the scheme swithes to first order, and the antiparallel components of the magnetic field dissipate at a rate that is some fraction of the local fast magnetosonic speed. While we cannot resolve the scales of the viscous shock layers or the current sheet width due to resistivity, the solution can still be reasonably accurate on larger scales. MHD models with numerical viscosity and
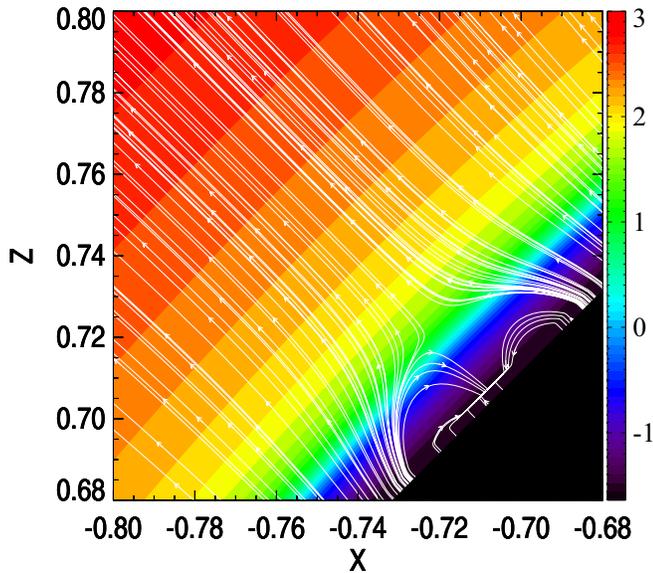
**Figure 1.** Cut-planes across the jet region show the initial collisional heat exchange timescale calculated in [s], plotted on a logarithmic scale. $X$ and $Z$ axes correspond to the HGR coordinate system; see discussion in the text. White lines show two-dimensional magnetic field lines.

resistivity have successfully simulated numerous space plasma systems with shocks and reconnection sites—see for instance the review by Tóth et al. (2012).

In our numerical scheme, the dissipated kinetic energy at shocks is being delivered to proton heating only. Another consequence of our numerical scheme is that for magnetic reconnection, the dissipated magnetic energy is being delivered only to the protons due to the conservation of the total energy that includes the proton thermal energy density. This is contrary to a reconnection based on resistivity, which would heat the electrons. In our model, the electron thermal energy is calculated from Equation (5), which involves adiabatic heating, heat conduction, and proton–electron heat exchange. That the protons are heated instead of the electrons is justified as long as the Coulomb collisional energy exchange equilibrates the electron and proton temperatures at a fast enough rate. In Figure 1, we show in a meridional slice through the jet region the timescale of the collisional heat transfer between the electrons and protons for the steady state at time $t = 0$ s. This shows that this timescale is small in this region, so that the proton and electron temperatures remain very close to each other. Hence, we assume that the imperfections of the adaptation of the physics into the global model do not have a significant effect on the resulting behaviour of the jets.

The initial and boundary conditions applied to these equations are discussed in Section 3.3.

### 3.2. Jet Model

In this paper, we present two jet scenarios, with one jet positioned at 90° and the other at 45° magnetic latitude with respect to the background solar dipole field. Throughout the paper, we refer to the jet in the open-field region at 90° as the "polar" jet, and to that in the tilted, closed-field region at 45° as the "loop" jet. The total solar magnetic field is represented by the superposition of a dipole positioned at the Sun's center to generate the weak, global background field and a dipole positioned at a small depth $d = 1.4 \times 10^{-2} R_\odot$ below the

Sun's surface and oriented in the radial direction to generate the stronger, more compact field of the jet source region. The global dipole field has a vertical strength of 2.8 G at its magnetic pole on the surface, whereas the compact dipole field has a vertical strength of 35 G. The two fields are oppositely directed at the surface above the compact dipole, forming a dome of closed magnetic flux with a magnetic null point at its top. As described in Section 2, multiple observations show that untwisting motions are quite common in jets, indicating that the jets likely originate in the interaction between twisted flux in compact magnetic loops and untwisted flux in the large-scale background field. To capture this feature, we initiate the jet by imposing a rotation of the chromospheric plasma at the base of the domain around the axis of the compact dipole field. Due to the flux-freezing condition of ideal MHD, the plasma motion drags the magnetic field along, inducing magnetic twist in the closed flux beneath the dome. A similar energization mechanism was used by Pariat et al. (2009, 2010, 2015) to initiate jets in Cartesian geometries. We adopted the simple analytic velocity profile

$$v_\perp = Ar - Br^C, \tag{13}$$

where $v_\perp$ is the tangential velocity of the plasma imposed on the boundary cells of the grid below the solar surface and $r$ is the radial distance of each point from the compact dipole's axis. To obtain a close match to the profile used by Pariat et al. (2009), we chose the parameter values $A = 3.60 \times 10^3\, R_\odot^{-1}\, \mathrm{km\, s^{-1}}$, $B = 2.42 \times 10^{11}\, R_\odot^{-C}\, \mathrm{km\, s^{-1}}$, and $C = 5.14$. The rotational motion is imposed between distances $0.002 R_\odot$ and $0.013 R_\odot$ from the dipole axis; at the outer edge of this range, $v_\perp$ falls to zero. These choices result in a peak velocity magnitude of $30\, \mathrm{km\, s^{-1}}$, which is approximately the chromospheric sound speed and less than 10% of the peak Alfvén speed within the dome. The magnetic field evolution, therefore, was reasonably quasi-static. Slower rotational motions would have been preferred, but they also would have made the simulations impractically long to perform. The rotational speed (approximately $33\, \mathrm{km\, s^{-1}}$) is just below the local ion acoustic speed and well below the local Alfén speed.

### 3.3. Boundary and Initial Conditions

Rather than simulating only a local wedge or box around the jet as most jet models do (Pariat et al. 2009, 2010, 2015; Fang et al. 2014), we solve the equations in three dimensions on a spherical domain, from the chromospheric inner boundary at $r = 1.001 R_\odot$ to the outer boundary at $r = 24 R_\odot$. All simulations were performed in a Heliographic Inertial Coordinate System, which in the case of the non-rotating solar body, is the same as Heliographic Rotating Coordinate System (HGR). The origin is in the center of the solar body, and the $X$ axis is aligned with the intersection of the ecliptic and solar equatorial planes. The $Z$ axis is perpendicular to the solar equator and directed north, and the $Y$ axis is completed according to the right-hand set. The zero latitude is positioned on the solar equator, positive on the northern and negative on the southern hemisphere. The zero longitude is towards the $X$ direction, and increases towards the $Y$ axis. In each figure panel, we indicate the orientation of the coordinate system in the bottom-left corner.

The boundary conditions imposed at $24R_\odot$ are super-Alfvénic outflow. The initial condition over the domain is the Parker solution with chromospheric boundary conditions $n = 3 \times 10^{10}\,\mathrm{cm}^{-3}$ and $T = 5 \times 10^4\,\mathrm{K}$ at $1.001R_\odot$. At the inner boundary, the boundary conditions are the following:

1. The radial magnetic field component $B_r$ is held fixed; the latitudinal and longitudinal components $B_\theta$ and $B_\phi$ are allowed to adjust freely in response to the interior dynamics.
2. The density $\rho$ in the boundary cells is fixed according to the exponential scale-height profile.
3. Both the proton and electron temperatures are fixed at the lower boundary to $T_{e,p} = 5 \times 10^4\,\mathrm{K}$.
4. The outgoing Alfvén-wave energy density $w_+$ is fixed to provide constant, continuous heating that sustains the atmosphere (see Sokolov et al. 2013 for details); the incoming wave energy density $w_-$ is set to zero.
5. The field-aligned velocity component $v_{\mathrm{par}}$ is copied from the first physical cells into the boundary cells (mirrored relative to the boundary); the other velocity components $v_{r \times B}$ are reflected.

In the chromospheric boundary grid cells the temperature is set to $T = 50{,}000\,\mathrm{K}$, while the density falls according to the exponential scale height, which provides a solution in hydrostatic equilibrium with gravity. The transition region is intentionally broadened (Lionello et al. 2009) so that it can be numerically resolved in a global-scale 3D model, and is lifted, along with the underlying chromospheric plasma, into the corona by the jet. The rotational boundary flows at the jet's location, described in Section 3.2, are superimposed on the velocity boundary conditions above. These flows introduce an additional Poynting flux of energy into the domain, augmenting the prescribed Alfvén-wave energy flux, which is the source of the magnetic energy injected as twist field and stored below the dome.

To avoid the singularity of the spherical grid at its poles, the jet region is placed at $45°$ latitude and $180°$ longitude. To obtain the open-field conditions for the polar jet setup, we aligned the axis of the global background dipole with that of the compact jet dipole. To obtain a background with a tilted and closed magnetic field around the loop jet, we aligned the global dipole axis with the $Z$ coordinate direction, as is usually done.

In our simulations, we used a second-order scheme with Linde flux and Koren limiter, setting $\beta = 1.2$ (for details, see Tóth et al. 2012). We keep the divergence of the magnetic field small by using the eight-wave scheme of Powell (1994). The radially stretched spherical block adaptive grid uses nine refinement levels resulting in 6 million cells. The simulated three hours of physical time required approximately 8 million iterations and took more than a half million CPU hours per simulation.

The initial solar wind solutions (before the jets are initiated) are presented in Figures 2 and 3. Figure 2 shows the radial velocity and magnetic field profiles in both configurations. The top-left panel shows the effect of the $45°$ rotation of the global dipole field on the solar-wind velocity profile for the polar jet; the bottom-left panel is the same view for the loop jet. In the middle panels, the small negative-polarity region (blue) on the upper hemisphere is due to the compact dipole field where we generate the jets. In the right panels, we show the initial magnetic structure near the jet dipole. The ambient magnetic field is weaker and tilted in the case of the loop jet (bottom) compared to the polar jet (top). Figure 3 shows the profiles of magnetic field strength, radial magnetic field component, density, pressures, and temperature ratio. The compact jet dipole has no significant effect on the steady-state solar wind solutions at global scales.

We first ran the simulations in local time-stepping mode for 80,000 iterations, during which we performed adaptive mesh refinement (AMR) on the inner shell of the domain close to the inner boundary, to resolve the high-density transition region and low corona. Once those solutions converged, we again performed AMR, but this time only close to the region where the jet dipoles are located: in a spherical box of $5°$ in both longitudinal and latitudinal directions and $0.1R_\odot$ in the radial direction. The resulting cell size in the jet region is about $1.4 \times 10^{-3}\,R_\odot$ in the azimuthal and $2.5 \times 10^{-5}\,R_\odot$ in the radial directions. We need such high resolution to fully resolve the jet structure. The grid for the polar jet is shown in Figure 4. On the left, we show the whole simulation domain; the middle and right panels focus on the jet region. The grid for the loop jet is similar. As jets have been observed to persist over long timescales (some jets inside active regions last for up to 10 hours; Savcheva et al. 2007), we carried out both simulations until the solutions become quasi-periodic in response to the ongoing rotational driving.

## 4. SIMULATION RESULTS

In this section we discuss the results of our simulations of both the polar and loop jets. Due to the similarities in the low-coronal structure and the driving mechanism in the two cases, numerous features of the resulting jets are shared by the configurations. On the other hand, because the polar jet occurs in an open magnetic field while the loop jet occurs in a closed field, other aspects of the two jets are distinctly different. We explore both their similarities and differences in the subsections to follow.

As described above, we began by relaxing both systems to a minimum-energy, quasi-steady state. Then, we initiated the steady footpoint driving within the closed magnetic flux of the compact dipoles. In each case, there followed an initial interval of buildup of magnetic twist within the closed regions, culminating in a first, energetic burst of reconnection and release of a jet. The systems then relaxed, but not all of the way back to their starting, minimum-energy states. Closed magnetic flux embedded deep within the jet source region was unable to transfer its twist to the ambient, untwisted open field by reconnection. This trapped twist flux and its associated magnetic free energy served as the starting configuration for a new cycle of constant footpoint motions, gradual energy storage, sudden onset of magnetic reconnection, and rapid release of another jet. These repetitive cycles quickly settled down to drive quasi-periodic recurrent jets in both of our configurations. We anticipated this outcome, based on the previous demonstration by Pariat et al. (2010) of homologous polar jets driven by similar footpoint motions in an adiabatic, Cartesian, gravity-free simulation. In our descriptions below, we focus on the properties of a typical quasi-periodic individual jet from each of our two cases, rather than on the unique, and somewhat atypical, initial jet. The most important new features of our simulations are the properties of the jet plasma, which we illustrate in the inner corona for both of our jets. Thereafter,
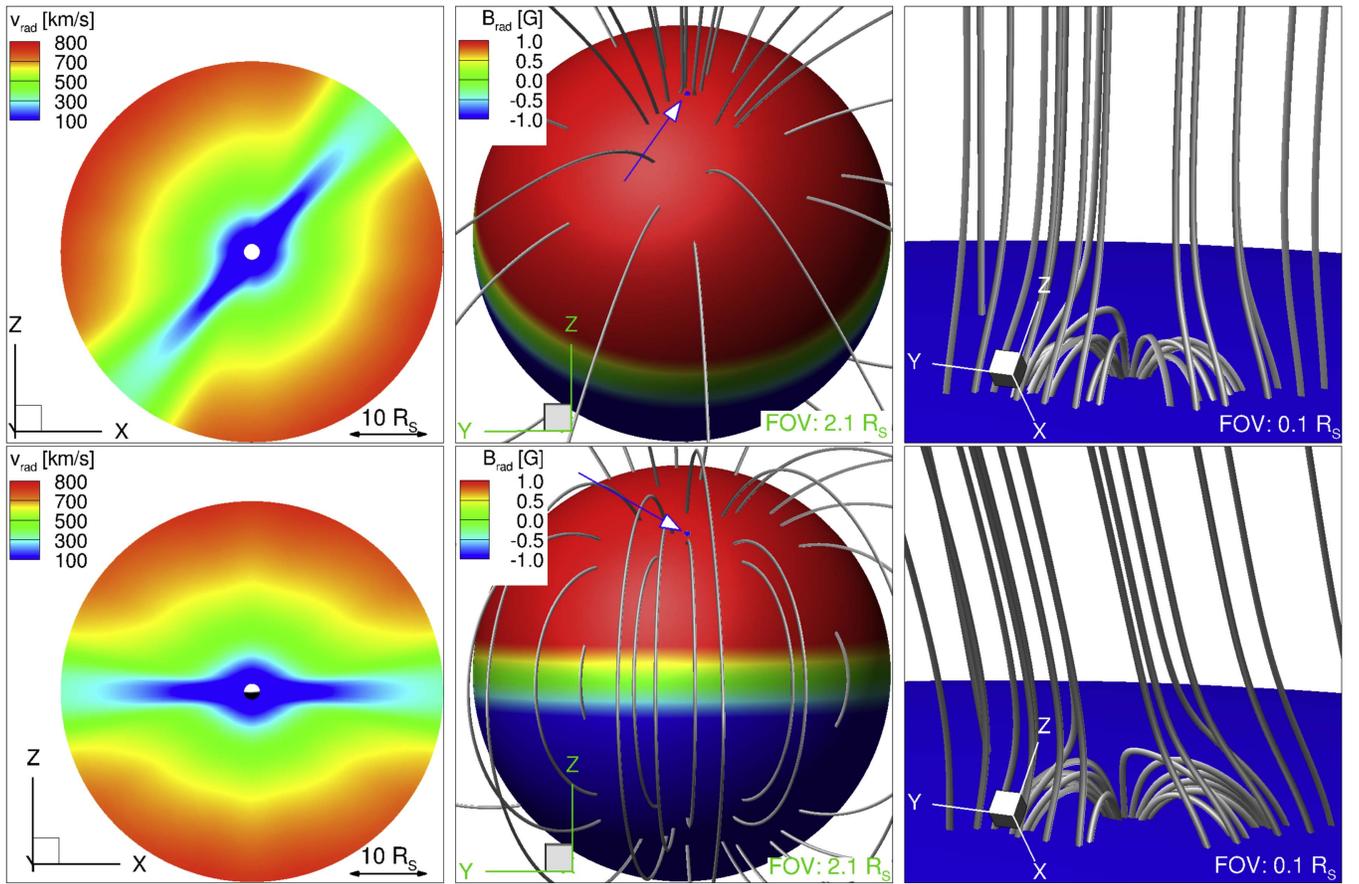
**Figure 2.** Initial configurations for the simulated polar jet in the vertical open-field region (top row) and the loop jet in the tilted closed-field region (bottom row). Shown are the radial velocity in the $Y = 0$ plane (left panels), the radial magnetic field on the solar surface $r = R_\odot$ with some representative field lines (middle panels), and a zoomed-in view at the jet location (right panels). The compact jet dipole is the small blue dot marked by the arrows on the upper hemisphere. The scales are indicated by the black arrows of the field of view (FOV), which define the physical size of the plotted regions. In the bottom-left corners we indicate the orientation of the coordinate axes of the images shown.

we examine the cumulative impact of the recurrent polar jets on the outer corona as well.

### 4.1. Jet Generation by Magnetic Reconnection

The ongoing process of jet generation by magnetic reconnection is illustrated in Figure 5 for the polar jet in the top row and for the loop jet in the bottom row. All panels show a fixed-time snapshot during one of the quasi-periodic bursts of reconnection between the twisted, closed flux of the compact dipole field and the untwisted, open (or, in the loop case, faraway closed) flux of the global dipole field. Within each row, the field lines labeled [1] and [2] are the same. The lines labeled [2] are strongly twisted field lines rooted to the chromosphere at both ends within the closed-flux region. They are pre-reconnection field lines adjacent to the separatrix surface of the compact dipole field. The lines labeled [1] are rather strongly bent and are rooted to the chromosphere only at one end and, therefore, belong to the open-flux region. They are post-reconnection field lines, also adjacent to the separatrix surface.

The field lines [1] pass through a vertical plane cutting across the jet (left panels), where color shading shows the strong reconnection outflows from the reconnection region. These flows start from the top of the closed-flux dome in both jets. We note that the outflow is stronger in the case of the polar jet throughout the simulation than at lower latitudes, because the

ambient magnetic field is stronger in the open-field region. The middle and right panels of Figure 5 show the rotating separatrix surface, which is color-shaded by the proton temperature. This surface is much hotter than the ambient plasma due to magnetic-energy release by the ongoing reconnection. The bent field lines [1] at the domes of the jets have newly reconnected and are still touching the locally heated separatrix surface. After a few seconds, they stretch and straighten out to become parallel to the ambient open field. The twisted field lines [2] also touch the separatrix surface and are about to reconnect with the ambient field to form new lines of type [1]. The visible twist and tilt on the open field lines, the heated spots on the separatrix surface, and the strong bidirectional outflows all highlight the locations of reconnection between the closed, twisted flux of the compact dipole source and the open, untwisted flux of the ambient field.

### 4.2. Temperature

The middle and right panels of Figure 5 show elevated temperatures occurring on the separatrix surface, reaching 20 MK for the polar jet (top row). As observed with SXT by Shimojo et al. (1996), the bright spot is expected to be above the footpoint of the jet region (see figures at Section 5): the localized heating takes place around the dome, especially close to its top, where the magnetic reconnection takes place. We show the proton temperature in Figure 5; because of the
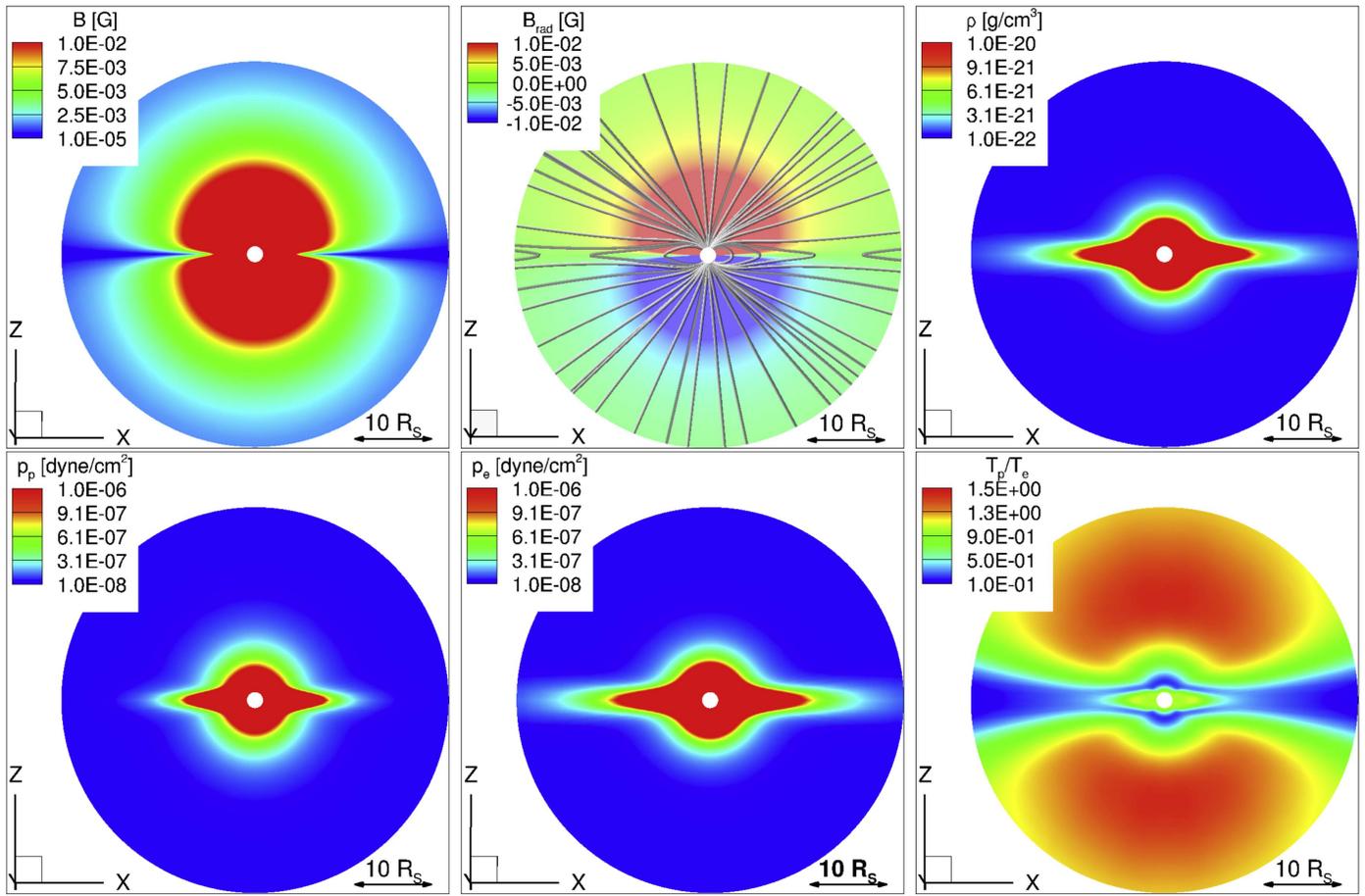
**Figure 3.** Loop jet initial condition on the $Y = 0$ plane. From left to right, top row: total magnetic field strength, radial magnetic field component with some magnetic field lines, and density of the steady-state solar wind. Bottom row: proton pressure, electron pressure, and temperature ratio of protons to electrons. See Section 3 for details on the model.

numerical scheme used in our model, the reconnection directly heats the protons, through Equation (4). Thermal energy is subsequently transferred to electrons via collisions, so the electron temperature responds with a time delay relative to the reconnection events that promptly heat the protons. This electron heating, in turn, has a profound effect on the radiative properties of the jets by determining which emission lines are excited and how intense are their emissions. Synthetic images of our simulated polar jet are compared with observations below in Section 5. (Synthetic images of the loop jet are similar to the ones presented.)

### 4.3. Density

The middle and right panels of Figure 5 also show gray isosurfaces of plasma at chromospheric density $\rho = 5 \times 10^{-15} \, \text{g cm}^{-3}$. This dense plasma has been lifted up to heights well above the ambient chromosphere, where it mixes with the tenuous coronal plasma. We also have identified complementary regions of highly depleted plasma density at very low heights, close to the footpoints (not shown). This density structure is similar to those observed, for example, with SXT by Shibata et al. (1992). Due to the quadratic dependence of the optically thin radiative losses on the plasma density, the enhanced densities at low coronal heights contribute very substantially to our synthetic emission images shown in Section 5 below.

As the twisted magnetic field in the closed region reconnects with the ambient field in the open region, the reconnection outflows depart along both field-aligned directions, upward and downward. The upward reconnection outflow continues to propagate along the field lines: radially in the polar jet and equatorward in the loop jet. Figure 6 shows the changes in the density profiles, relative to the steady-state corona, for both jets. A strong density enhancement extends to several solar radii in the polar jet, while the jet material crosses the equator to reach the other hemisphere in the loop jet. We note that our polar jet contributed density enhancements over 10 times greater than the ambient coronal value after expansion into the outer corona. These values are far larger than those observed in the adiabatic or isothermal simulations of Pariat et al. (2009, 2010, 2015) or Karpen et al. (2016), respectively, none of which included the effects of the underlying chromosphere on the jet density. Pucci et al. (2013) observed the density enhancements of standard and blowout jets to be about $10^{-16}$–$10^{-15} \, \text{g cm}^{-3}$, which in magnitude corresponds to the density of the lifted chromospheric plasma in our simulations.

### 4.4. Velocity

As described in Section 3, the rotation around the bipole axis is imposed on an annulus at the lower boundary. This implies that the magnetic field lines crossing the surface in the center of the annulus (close to the axis of the compact dipole) have one
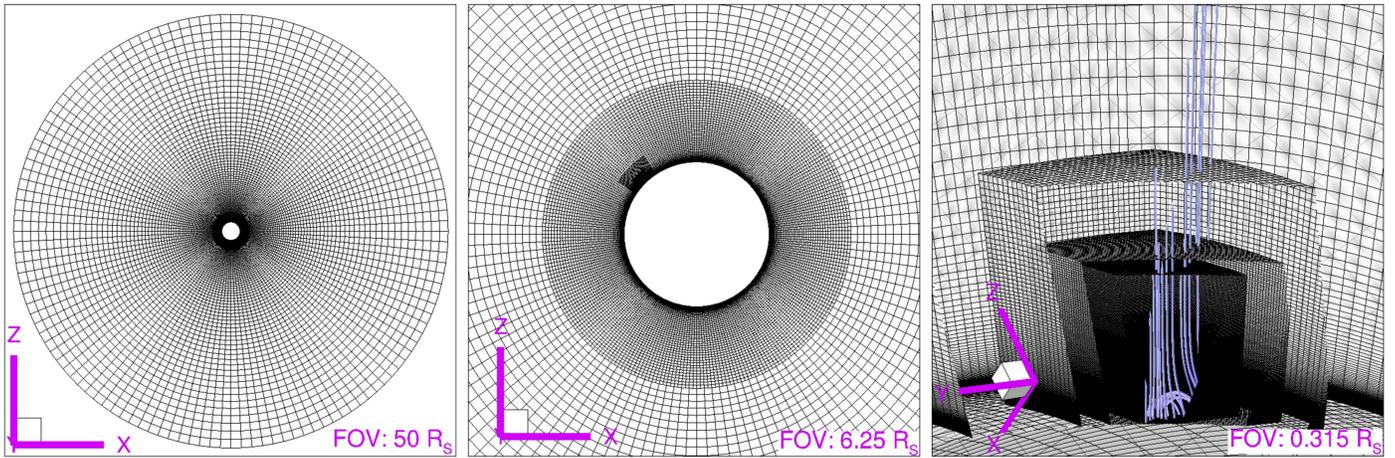
**Figure 4.** Left: grid structure in a 2D cut at $Y = 0$ of the whole domain ($24R_\odot$). Middle: same, zoomed to $6.25R_\odot$, showing the first few levels of the adaptive, radially stretched grid. Right: zoomed to $0.3R_\odot$, showing several magnetic field lines near the jet dome.

footpoint fixed, while the other rotates along with the plasma. These magnetic field lines become tilted and twisted until they reconnect with the ambient field. As both the rotation and the reconnection are ongoing processes throughout the simulation, they introduce a quasi-periodic behavior into the system. In particular, they introduce periodic velocity and magnetic disturbances that travel outward along the magnetic field lines. This periodicity appears in the velocity profiles as Alfvénic perturbations. These are visible in Figure 7 as torsional waves propagating along the field lines.

### 4.5. Flows, Fields, and Forces in the Outer Corona

We now turn to the larger-scale effects on the outer corona of our simulated jets. Because the loop jet leaves signatures only relatively near the solar surface in the inner corona, in the remainder of this Section 4 we discuss in detail only our polar jet simulation. In case of the loop jet the closed-field geometry traps the jet outflow. Detailed analysis of the loop jet is left to be discussed in a future paper.

The physical size of this jet (length and width) is similar to what Savcheva et al. (2007) reported, although in their study there were some even larger jets observed in both dimensions. Due to the radial geometry of field lines, the polar jet leaves a stronger signature in the ambient plasma than the loop jet. In the polar jet case, the disturbances reach the outer corona beyond $20R_\odot$ by the end of the three hours of simulation time. This translates to an average wave speed of about $1300\ \mathrm{km\ s^{-1}}$; the jet plasma outflow is much slower (see later). Figure 8 shows the change introduced by the polar jet in the velocity, magnetic field, and Lorentz force profiles by the end of the simulation, on a global scale. As in the case of the jet driven by the helically twisted magnetic field described by Shibata et al. (1992) and confirmed via MHD simulation by Fang et al. (2014), the acceleration force is the Lorentz force as the magnetic twist propagates along the field lines. Wang et al. (1998) looked for jet signatures in the corona using simultaneous observations by LASCO and the Extreme-ultraviolet Imaging Telescope (EIT), both on board *SOHO*. They correlated 27 jet events observed by both instruments by following the jet lifetime from the appearance of bright points in EIT up to above three solar radii. The bulk material followed the leading edge of the jet at a smaller speed, decelerating below two solar radii. As a result, the jet plasma signature

became elongated in coronal plasma, just as it is shown in Figure 8. In the top, we see that the radial solar wind speed decreased, and also there are flows diverging from the jet towards the equatorial region. The middle row shows that the radial magnetic field increases in a large area in the outer corona, and it is strongly depleted close to the jet. Due to the radial dependence of the magnetic field strength, calculating the energy change in the region is highly dominated by the lower, depletion region. This is why the magnetic energy overall decreases in the coronal region, as discussed in Section 4.6. In the latitudinal and longitudinal fields, we see the periodic perturbation propagating outwards. In the bottom row, we show that Lorentz forces accelerate plasma radially (mostly) outwards, and also towards the equatorial regions, in a periodic-twisting manner.

### 4.6. Mass, Momentum, and Energy Transport

In order to provide an overall estimate of the polar jet contribution to the solar wind, we calculate the mass, momentum, and energy transport from the chromosphere into the corona across the jet area throughout the simulation. Paraschiv et al. (2015) used a sample of 18 jet observations to conclude that radiative and conductive losses are negligible. Also, calculating the wave energy and radiative loss terms, we observe no significant change to the background solar wind due to the jet. For this reason, we calculate the integrals of mass density, momentum density, and the magnetic, gravitational, internal, and kinetic energy densities, omitting wave energy and radiative losses. The integrations are performed every 10 seconds throughout the simulation within two fixed, over-lapping volumes shown in Figure 9. The first region (left panel) is selected to contain the core of the jet. Its extents are [43°, 47°] in latitude, [178°, 182°] in longitude, and [1.001, 1.030] $R_\odot$ in radius. We refer to this region as the "core," and use this volume to calculate and identify local effects of the rotation that take place in the jet-generation region.

The extents of the second region are selected so that the velocity perturbations propagating due to the jet into the outer coronal plasma are fully contained within the volume (middle panel). This region covers [15°, 75°] in latitude and [130°, 230°] in longitude. Since we want to obtain a direct estimate of the jet's contribution to the solar wind, the mass, momentum, and energy transfers are calculated considering only the coronal
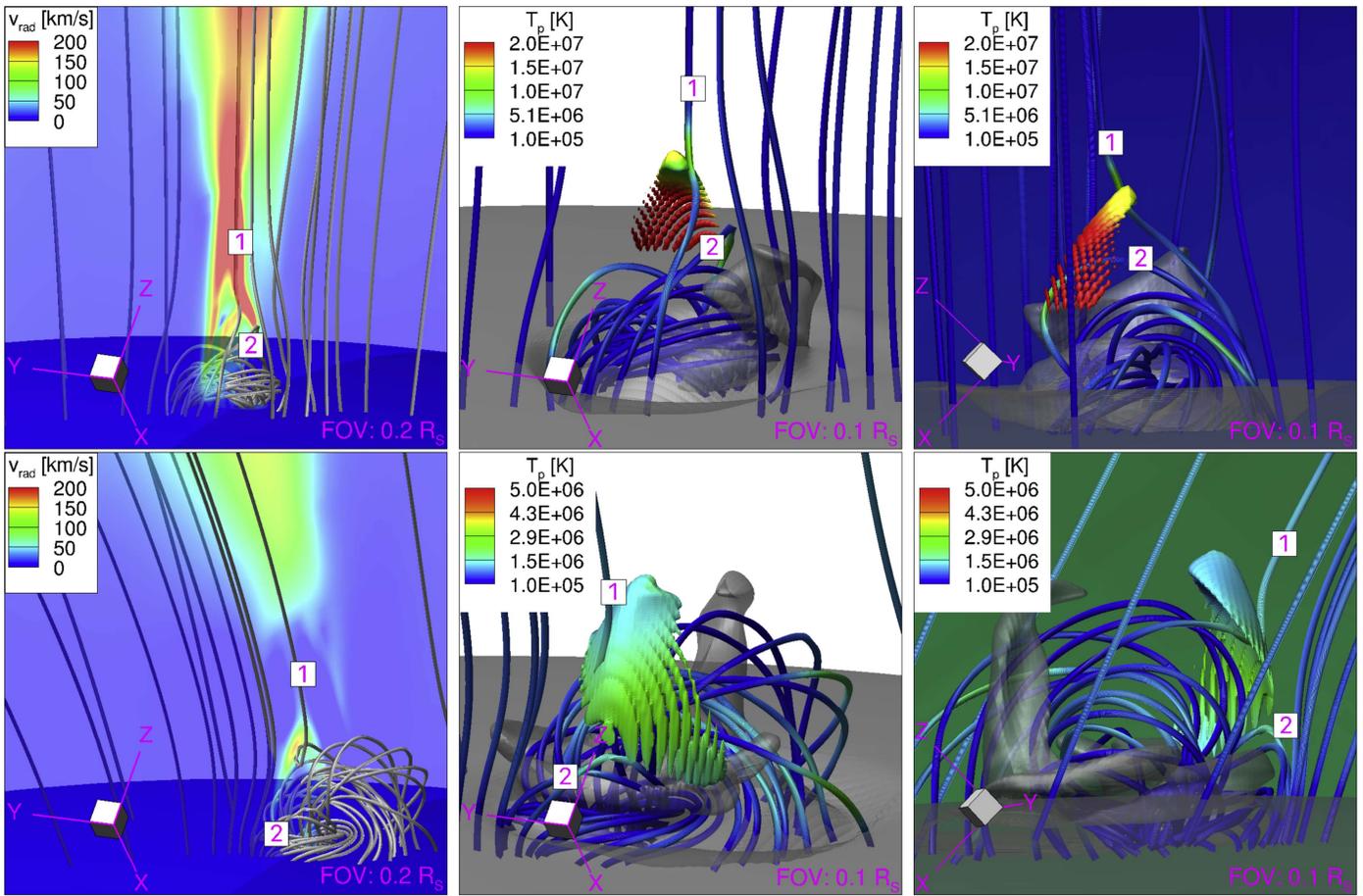
**Figure 5.** Polar jet simulation at time $t = 1$ h 27 m 20 s (top row); loop jet simulation at time $t = 2$ h 27 m 30 s (bottom row). Left panels: radial velocity is color-shaded on a plane through the center of the jet; gray and blue lines represent magnetic field lines in front of and behind the plane, respectively. Middle and right panels: zoomed to the jet core at the same times, from different perspectives. Magnetic field lines and the null-point region on the separatrix surface ($B = 0$ isosurface) are color-shaded according to proton temperature. Shown in transparent gray is an isosurface of dense plasma ($\rho = 5 \times 10^{-15}$ g cm$^{-3}$). Selected pre- and post-reconnection magnetic field lines are labeled [2] and [1], respectively.

plasma above $1.015R_\odot$ (the black line on the right panel of Figure 9) out to the far end of the domain at $24.0R_\odot$. We refer to this region as the "corona."

We show the enhancements of mass, momentum, and energy relative to the steady state in Figure 10 for both volumes. In the core of the polar jet, a substantial amount of dense plasma is lifted up from the chromosphere into the core region. This plasma passes through the core volume and then gets released into the coronal region. Comparing the changes in the total and gravitational energy within the core, we find a strong correlation between them. The same dynamics can be observed in the top and middle panels showing the mass and momentum changes. The panels showing the mass change in the corona indicate that the region is not yet filled with the dense plasma, but those in the middle row show that the rate of momentum growth decreases by the end of the simulation time. This suggests that either the plasma starts to reach the outer boundary, leaving the simulation (and integration) domain, or the plasma might get released in a decelerating manner due to the increasing local density. In the polar jet, after the first energetic reconnection event, the magnetic energy is reduced in the coronal region due to the field relaxation close to the jet core (Figures 8 and 11). Internal and kinetic energies converge to roughly constant values, with the kinetic energy reaching those values more slowly and remaining slightly below the

internal. Also during the first reconnection event, strong downward flows decelerate the otherwise radially outward moving plasma, which causes a large decrease in the kinetic energy at around $t = 1000$ s. This event resembles the pulse-driven jets discussed by Srivastava & Murawski (2011). The driver is most likely a single velocity pulse generated by the magnetic reconnection in the lower atmospheric region, although we did not observe cool plasma falling back after the ejection, as seen in observations.

Looking at the mass and momentum changes in the core over time, the phases of the jet dynamics described by Pariat et al. (2010) clearly appear: the energy build-up in the first approximately 1000 s, then the violent energy release, followed by a relaxation to a quasi-periodic state. A typical X-ray jet of size $5 \times 10^3$–$4 \times 10^5$ km has kinetic energy about $10^{25}$–$10^{28}$ erg (Shibata et al. 1992). Our jet model fits into both ranges. We estimate the internal energy and mass transport into the corona through our polar jet model to be $6 \times 10^{13}$ g in the core, and $7 \times 10^{14}$ g in the corona. Shibata et al. (1992) also estimated these values in the case of a jet driven by a helically twisted magnetic field. The internal energy was about an order of magnitude larger than the kinetic. The mass of the observed jet was estimated to be around $10^{13}$ g. We see that the change of gravitational energy dominates both volumes, followed by magnetic energy in the core of the
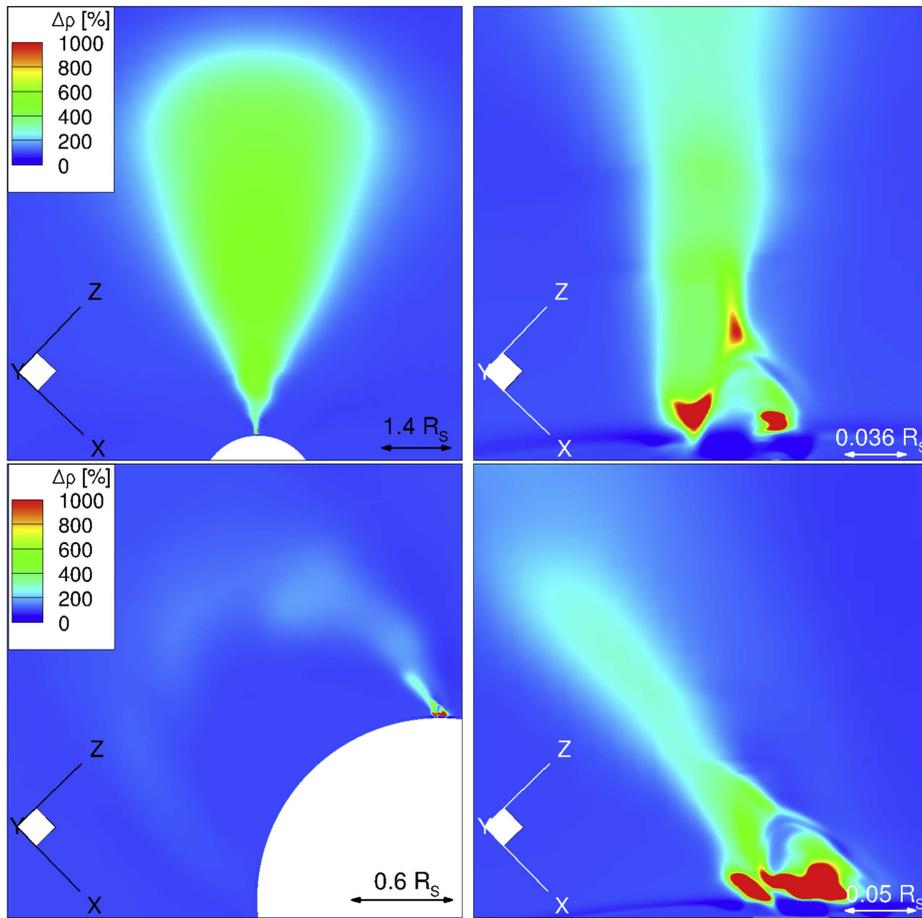
**Figure 6.** Density enhancement relative to the initial steady state in planes through the center of the polar (top row) and loop (bottom row) jets. Left panels: large-scale view of the solar wind; the partial white disk is the Sun. Right panels: close-up view near the solar surface.

jet, and internal and kinetic energies within the coronal volume. These results are consistent with the observational study done on 18 jets by Paraschiv et al. (2015), finding that plasma heating takes a larger share of the energy than plasma acceleration.

### 4.7. Quasi-periodic Recurrence

We observe two oscillatory behaviors: faster fluctuations superimposed on oscillations with longer periods. The large amplitude oscillations observed in the core appear mostly in the mass change rate, but they leave much weaker signatures in the energy terms compared to the small amplitude ones. Besides the three large-scale peaks in density, momentum, and gravitational energy at time instances around $t = 1000$ s, 5000–7500 s, and 8000–10,000 s, there are oscillations at a smaller timescale, visible in all variables shown in Figure 10. There is a strong correlation between mass change, momentum change, gravitational, kinetic and internal energy changes, and a strong anti-correlation between these and magnetic energy changes. These oscillations are clearly due to the continuous quasi-periodic reconnection process that creates the plasma perturbations shown in Figure 8. The oscillatory behavior is driven by reconnection events where the magnetic field direction changes sufficiently rapidly. The periodicity of these events is governed in part by the local value of the numerical resistivity (as discussed in Section 3.1), and in part by the rate of formation and strengthening of the current structures in

response to the imposed surface motions, which together determine the onset and conditions and rate of reconnection. The approximate period of these oscillations is about 700–800 s.

Chifor et al. (2008a) also observed recurring solar jets in X-ray and EUV bands with periodicity of about an hour. Flux cancellation (with a minimum magnetic energy loss per jet of about $3 \times 10^{29}$ erg) was correlated with the brightenings observed in X-ray and Ca II H. The same magnitude of total energy transported into the corona is produced by our model. Chifor also observed type III radio burst signatures during the first two largest jets, suggesting that stronger reconnection events happened at the beginning of the jet process, compared to later occurrences.

As discussed in Section 3.2, we impose a differential rotation profile in the boundary cells with peak rotation speed 30 km s$^{-1}$ at distance $0.0085R_\odot = 5950$ km from the bipole axis. The plasma completes one rotation every 1246 s, corresponding to 8.86 rotations during the 11040 s simulation time. The system stabilizes after the first energetic reconnection at around $t = 3000$ s. Until $t = 10,500$ s of the simulation, we observe about 10 complete small timescale oscillation periods (inferred from Figure 10). This gives us an average period of 750 s. The period of reconnection events is about half of the rotation time period. Shen et al. (2011) used AIA observations and discussed rotary motion and radial expansion on one side of the polar jet. They observed a mean rotational period of about 564 s. The twist stored before reconnection was between
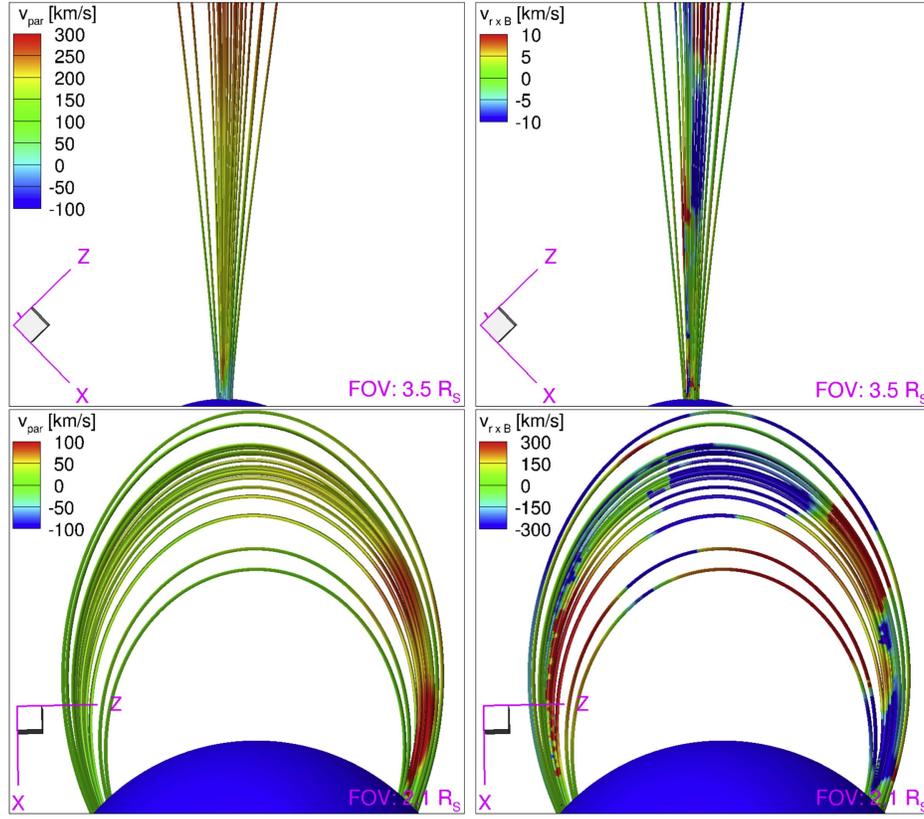
**Figure 7.** Plasma velocities for polar (top row) and loop (bottom row) jets color-shaded on selected magnetic field lines at the end of the simulations. Left panels: field-aligned component ($v_{\mathrm{par}}$). Right panels: perpendicular component ($v_{r\times B}$). The perpendicular component is projected along the cross product of the position vector $r$ with the magnetic field $B$, to distinguish positive and negative directions.

1.17 and 2.55 turns, which matches theoretical and simulated results. Our jet shows more frequent reconnections and hence, it stores less twist. We suspect that the reason for this difference is that we use a second-order numerical solver, which corresponds to relatively high numerical resistivity. Using a numerical solver of higher order would decrease the numerical resistivity and may lead to more twist being stored between the reconnection events.

### 4.8. Energy Changes in the Corona

Shen et al. (2011) estimated the stored magnetic energy to be approximately $(0.7–3.4) \times 10^{30}$ erg, and the jet's total hydrodynamic energy (kinetic, internal and gravitational) to around $1.7 \times 10^{29}$ erg. Our simulated energies are at the same magnitudes as their estimate, suggesting that the modeled energy transport into the solar corona is consistent with observations.

The surface of energy deposition is a $2° \times 2°$ square (latitudinal × longitudinal width). We integrated the Poynting fluxes in the first physical cells either due to both Alfvén-wave dissipation and plasma motion in the changing magnetic field. The integration box was selected to be the smallest possible containing the base of the jet structure. In this small region, we find that the average energy deposited in the boundary due to Alfvén-wave dissipation was about 271 and 2490 erg cm$^{-2}$ s$^{-1}$ due to plasma motion. All plasma motions are included in the energy flux calculation, including interior flows or waves that impinge upon the boundary and alter the imposed flow. These values are hence considered only a time average of Poynting fluxes related to the jet in the regions.

The imposed rotation generates Alfvén waves. As the energy panels in Figure 10 show, the energy deposited in the corona is mostly due to the plasma outflow and heating, rather than magnetic energy. Looking at the panel of the core energy changes, we see that substantial magnetic free energy is stored in the jet and the reconnection process significantly changes only the gravitational, internal, and kinetic energies, not the magnetic energy itself. We conclude that the magnetic energy released in a reconnection event is only a small fraction of the magnetic energy stored within the jet-producing region.

As will be shown below, the gravitational energy is dominant in the core, due to the large relative density enhancement shown in Figure 6. Looking at a cut-plane across the jet in Figure 11, the temperature and energy change significantly in the domain relative to the initial state of the solar wind. There is a visible jump in each energy profile at about $9R_\odot$, where the density enhancement region (relative to the original value) ends (see Figure 6, top right). At this height, the relative change in the plasma beta jumps from positive (in the low corona) to negative (in the outer corona). This jump is a consequence of the Alfvén-wave heating, which is based on Equation (6). The reflection rate $\mathcal{R}$ introduced in Equation (6) is a key parameter understanding how the energy is deposited in the disturbed coronal region. Following the derivation of van der Holst et al. (2014), the evolution of parallel and antiparallel Alfvénic waves is governed by a balance between reflection $\mp\mathcal{R}\sqrt{w_-w_+}$ and dissipation $-\Gamma_\pm w_\pm$:

$$\mathcal{R} = \mathcal{R}_{\mathrm{imb}}\left(1 - 2\sqrt{\frac{w_-}{w_+}}\right), \qquad (14)$$
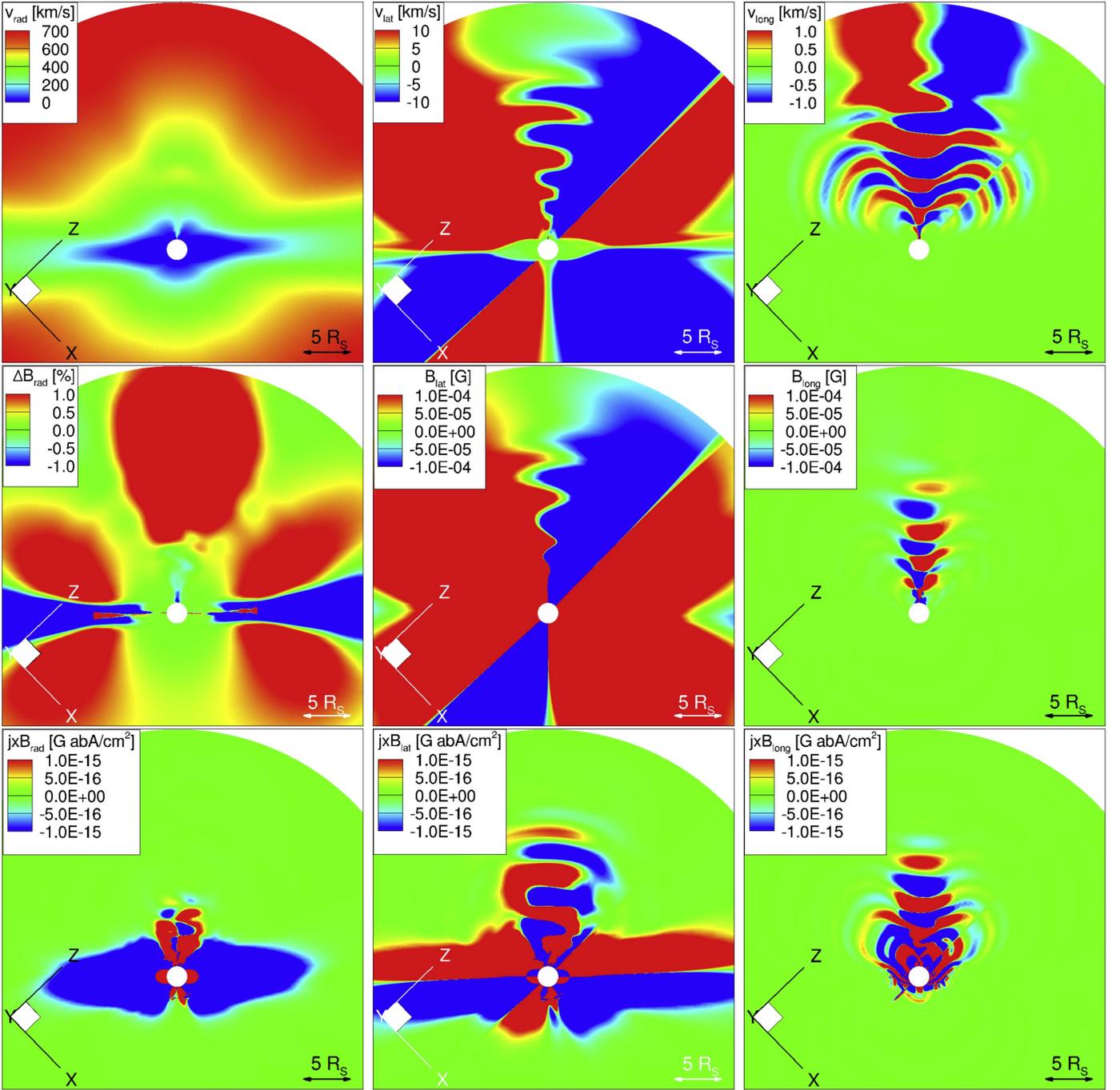
**Figure 8.** Polar jet at the end of the simulation. Top row: radial, latitudinal, and longitudinal velocity components (left to right). Middle row: radial magnetic field change (left) and latitudinal and longitudinal magnetic field components (middle and right). Bottom row: radial, latitudinal and longitudinal components of the Lorentz force (left to right). All figures show the same plane through the center of the jet. The white disk is the Sun.

where

$$\mathcal{R}_{\mathrm{imb}} = \sqrt{(\boldsymbol{b} \cdot [\boldsymbol{\nabla} \times \boldsymbol{u}])^2 + ([V_A \cdot \boldsymbol{\nabla}] \log V_A)^2} \qquad (15)$$

and

$$\Gamma_{\pm} = \frac{2}{L_{\perp}} \sqrt{\frac{w_{\pm}}{\rho}}, \qquad (16)$$

and $L_{\perp}\sqrt{B} = 1.5 \times 10^9$ cm G$^{1/2}$ is an input parameter. The reflection and dissipation rates strongly depend on the local mass density, the magnetic field strength and direction, and the gradients of those variables. We consider only the form of

reflection rate in the case of imbalanced turbulence, on the northern hemisphere of the Sun, along straight magnetic field lines, where $4w_{-} \leqslant w_{+}$, as this region basically overlaps the hemisphere the polar jet interacts with. The dominant energy density outwardly propagating (parallel) wave is more than 100 times greater than the counter-propagating (antiparallel) one in this region, so we assume strongly imbalanced turbulence and local wave dissipation. During the simulation, the reflection rate increases due to the introduced Alfvén speed gradients and velocity vorticity along the radial flow direction (Figure 8). With the increased reflection rate, the turbulence gets more
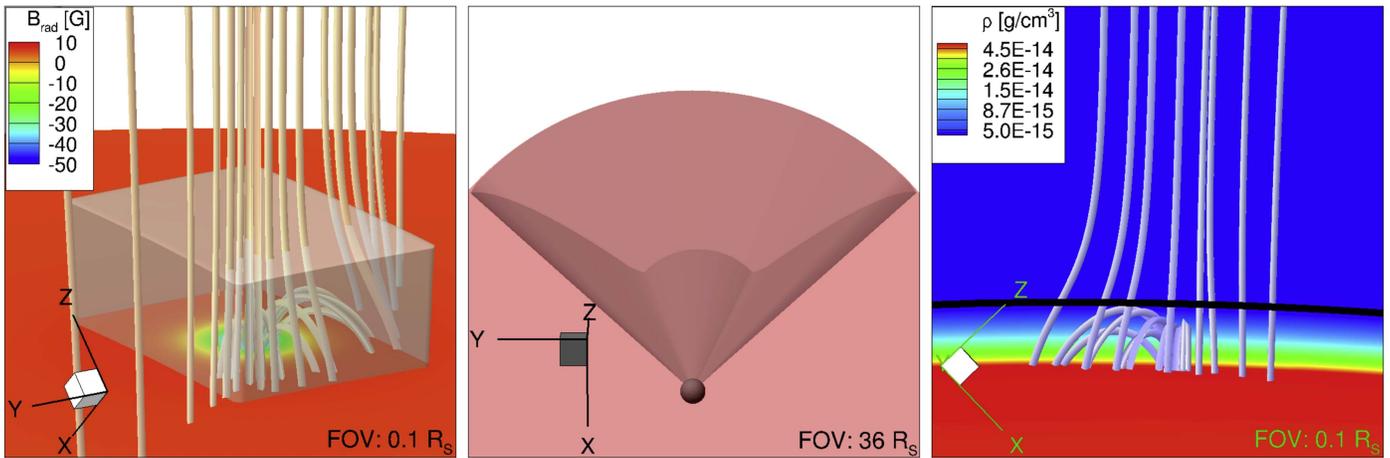
13

**Figure 9.** Integration regions for the polar jet. Left panel: the core integration region is the translucent box. The radial magnetic field component on the solar surface is color-shaded; selected magnetic field lines are shown. Middle panel: the coronal integration region is the pink-shaded volume. Right panel: plasma density is color-shaded near and on the solar surface. The black line marks the lower boundary of the coronal integration region at $1.015R_\odot$; the chromosphere is excluded from this region.

balanced, and there are more inwardly propagating waves. The interaction between the oppositely propagating waves results in higher energy dissipation rates. This means that where the reflection rate has a sharp gradient (where the density-enhanced region ends), there is a discontinuity in the rate of energy deposition. The result of this sharp gradient is shown in Figure 11: the lower region takes all the energy and inhibits heating above it. Within the region of large reflection rate, the corona is over-heated relative to the initial condition. Due to the way the traveling Alfvén waves are trapped within the region, the energy deposition is decreased in higher radial distances from the region. This can be an indication of why there is a strong gradient in temperature and energy change in the corona. There is another strong gradient we see in the proton temperature: it corresponds to another sharp gradient in the reflection rate. The outer boundaries of these regions are propagating radially outward during the simulation, with a speed of approximately $325\,\mathrm{km\,s^{-1}}$. Overall, the integral of energy changes are highly biased by the low-coronal region because the changes are much more significant there than in the upper regions, as the strong fields reconnect in the lower region. This is why the overall budget for each energy variable becomes positive in the end. As *Solar Probe Plus* is going to fly through regions as low as 9 solar radii above the surface, the large gradients in density and temperature could be captured by measuring proton and alpha-particle properties.

The signatures of jet contribution to coronal heating and solar wind plasma were studied by looking for asymmetries (blueshifts) in the hot lines with EIS by Brooks & Warren (2012). They found that the outflow had a high-speed component, which might be a contributor to the slow solar wind based on the composition (FIP) of the wind. Also they noted that the released material was previously stored in coronal loops and was released by interchange reconnection between open and closed-field lines, which is the scenario in our model. Poletto et al. (2014) estimated the wind energy flux of the order of $10^5\,\mathrm{erg\,cm^{-2}\,s^{-1}}$, which for the whole Sun means a $5 \times 10^{32}\,\mathrm{erg\,day^{-1}}$ energy output. Our polar jet simulation contributes $5 \times 10^{29}\,\mathrm{erg}$ of energy in about

$1.1 \times 10^4\,\mathrm{s}$ simulation time through a surface of size $60°$ in latitude $\times 100°$ in longitude, that is, about $7500\,\mathrm{erg\,cm^{-2}\,s^{-1}}$ flux to the coronal volume. This contribution is about two orders of magnitudes smaller than Poletto's estimated solar wind energy output.

If we assume 50 jet events, each lasting for $1200\,\mathrm{s}$ (first blowout of energy occurring at about $10^{29}\,\mathrm{erg}$, as Poletto estimated), the 50 modeled polar jets contribute to the energy of the solar wind by about $5 \times 10^{30}\,\mathrm{erg}$, which is about $0.5\%$–$1\%$ of the overall energy budget needed to maintain the solar wind. We conclude that having several ongoing jets in both polar and lower latitudinal open flux regions would produce a couple of percent of the energy flux of the steady-state coronal value, which is similar to the result of Poletto et al. (2014).

## 5. COMPARISON WITH OBSERVATIONS

This section focuses only on polar jets. Even though we do not aim to model or reproduce any particular jet observation, we calculate line-of-sight images in the EUV and soft X-ray bands using CHIANTI tables of the temperature response functions of the AIA and XRT instruments, in order to identify comparable structures to actual jet observations. We selected three observations of jets having clear geometric structures and corresponding publications that played a main role in understanding our simulation results. They are the following:

1. Jet 1 occurred on 2007 January 17 at UT 13:15, was observed by XRT, and was studied by Cirtain et al. (2007). We compare our simulations to XRT images taken with the Al-poly filter. The temperature magnitude where the instrument is the most sensitive is around $T = 6.3 \times 10^6\,\mathrm{K}$. The original observations showed jets ejecting plasma at sound and Alfvén velocities. It was also suggested that jets are more common structures on the solar surface than suggested before the *Hinode* observations. These jets lasted longer than the chromospheric ones ($1000$–$2000\,\mathrm{s}$) and showed transverse oscillations with larger periodicity ($200\,\mathrm{s}$), suggesting Alfvén-wave generation during the reconnection processes. These XRT observations are part of the many images taken of the south pole during the *SOHO/Hinode* campaign 7197, analyzed by Savcheva et al. (2007). The
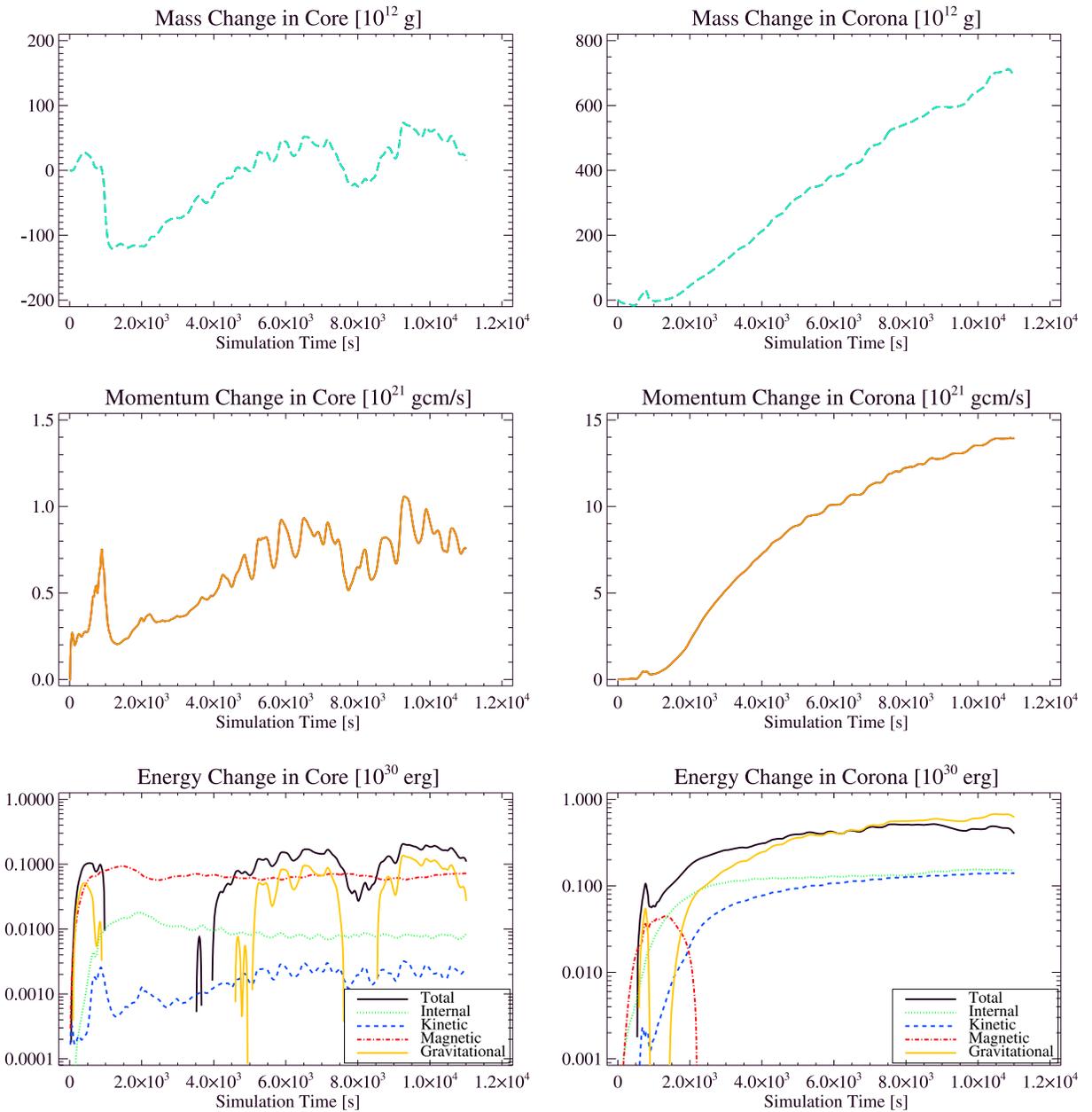
**Figure 10.** Integration results for the polar-jet core (left panels) and corona (right panels): changes in mass (top row), radial momentum (middle), and energies (bottom). Negative values of changes in the energies are not shown due to the logarithmic scale. See Section 4.6 for details.

resulting statistical study of X-ray polar jet parameters provided invaluable information on the velocity, size, location, and duration of jets. Here, we note that our simulation fits into the outward velocity range $(70–400 \, \mathrm{km \, s^{-1}}$, sometimes up to $1000 \, \mathrm{km \, s^{-1}})$ and the width range $((6–10) \times 10^3 \, \mathrm{km})$ estimated in that statistical study. The reported height range $((1–12) \times 10^4 \, \mathrm{km})$ strongly depends on the brightness of the ambient coronal plasma, but both our jet model and observations have rather comparable sizes as shown in Figure 12. Also in our case, we consider one period of about 700 s in duration. We are within the distribution of the observed jet period interval, which peaked at about 600 s, but ranged between 300 and 2500 s.

2. Jet 2 occurred on 2010 August 11 at UT 19:00, was observed by AIA, and was studied by Adams et al.

(2014). We compared images in bands 171 Å, 335 Å, and 131 Å, which are respectively sensitive to electron temperatures (for emitting ions) $T = 6.3 \times 10^6 \, \mathrm{K}$ (Fe IX), $T = 2.5 \times 10^6 \, \mathrm{K}$ (Fe XVI), and $T = 4 \times 10^5 \, \mathrm{K}$, $1 \times 10^7 \, \mathrm{K}$, and $1.6 \times 10^7 \, \mathrm{K}$ (Fe VIII, Fe XX, and Fe XXIII). These observations show the difference between jet models introduced by Moore et al. (2010) and the observed macrospicule jets initiated most likely by converging flows along supergranule edges. Also, they found that the observed blowout jet material was most likely stored within a magnetic arcade before eruption.

3. Jet 3 occurred on 2011 May 31 at UT 21:45, was observed by AIA, and was studied by Chandrashekhar et al. (2014). We use bands 193 and 211 Å, whose wavelength bands are dominated by emission from
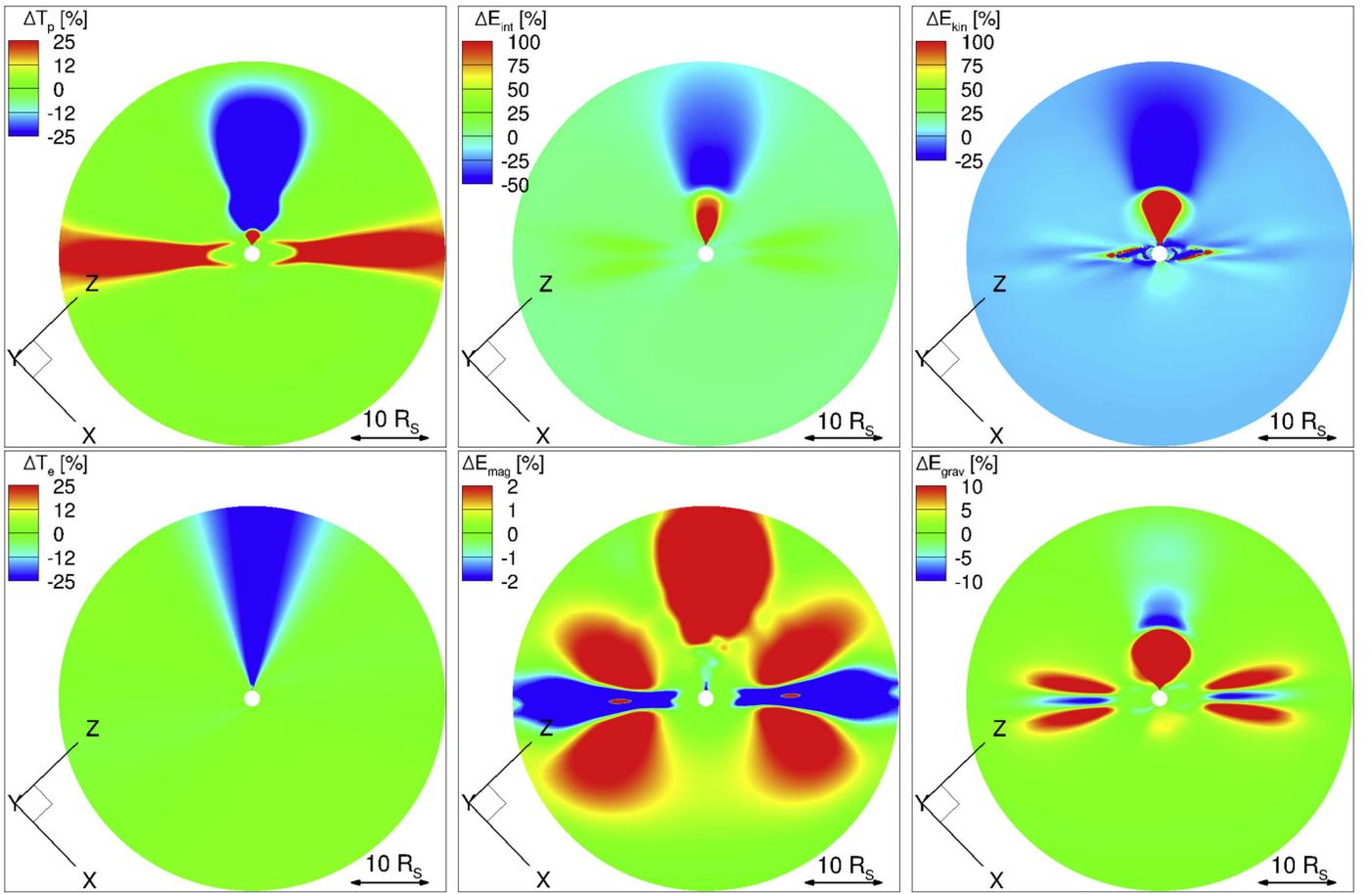
15

**Figure 11.** Temperature and energy-density changes for the polar jet at the end of the simulation. Top row, left to right: proton temperature, internal energy density, and kinetic energy density. Bottom row: electron temperature, magnetic energy density, and gravitational energy density. All figures show the same plane through the center of the jet as in Figure 8. The white disk is the Sun.

plasma at temperatures $T = 1.3 \times 10^6$ K, $2 \times 10^7$ K (Fe XII, Fe XXIV), and $T = 2 \times 10^6$ K (Fe XIV), respectively. These observations showed that as plasma flows along loops at the base of the jet, there are manifestations of quasi-periodic plasma ejections. There are transverse or rather torsional motions observed, interpreted as Alfvénic wave propagation with speeds over $100 \, \mathrm{km \, s^{-1}}$. The waves are also strongly damped during propagation, possibly due to a large density gradient between the initial and jet plasma (consistent with our model; see Section 4.5).

All synthetic images are generated for the full length of the simulation, every 10 s. The dynamics after the first stronger reconnection event are quite periodic. We see plasma spiraling from the disk-view images and periodicity in the location of bright points on the limb ones. We compare the polar jet model outputs at different simulation times to the selected observations. We show the images on the same spatial scale: the model jet is about the size of the observed one in each case. The coronal hole in the model (which simply corresponds to the pole of the dipole field; see Section 3) creates a cooler ambient plasma than the observed one: the computed coronal brightness is consistently closer to the observed one in the lower temperature bands. This also means that at very high temperature bands (X-ray) we are able to identify features more easily. Note that the extending base and the structure of a

mini filament are apparent next to the bright spot (at all wavelengths and jets), just as observed by Sterling et al. (2015). However, the model does not produce cooled plasma falling back to the region after ejection as observed (Culhane et al. 2007), but rather downward flows of the reconnection exhaust. The results are presented in Figures 12 and 13.

In Figure 12, the top row compares the jet model at $t = 1$ h 51 m to the observations of Jet 3 made at 21:45:57 UT for the wavelength band at 193 Å, and the middle row shows a comparison at 21:45:49 UT for the band at 211 Å. These iron lines correspond to plasma hotter than 1 MK. In this case, the jet model reproduces the dome shape and the asymmetry in intensity, but in size, it is larger by about 60%. Due to the background structures in the plasma, there is only a weak indication of the jet tail in the observations, unlike in the synthetic images, where the fully open field background is colder. Finally, on the two panels in the bottom row, we show an X-ray synthetic image of the model at $t = 1$ h 22 m 40 s compared to the observation of Jet 1 by XRT with an Al-poly filter at 13:19:07 UT. These images are on the same spatial scale. The dome structure and jet tail are very similar to the observed ones both in size and in intensity. Also, the bright footpoint on the left is visible and comparable in size in both images.

In Figure 13, the top two rows show a comparison of the jet model at $t = 2$ h 29 m (left) to Jet 2 at 19:02:13 UT at
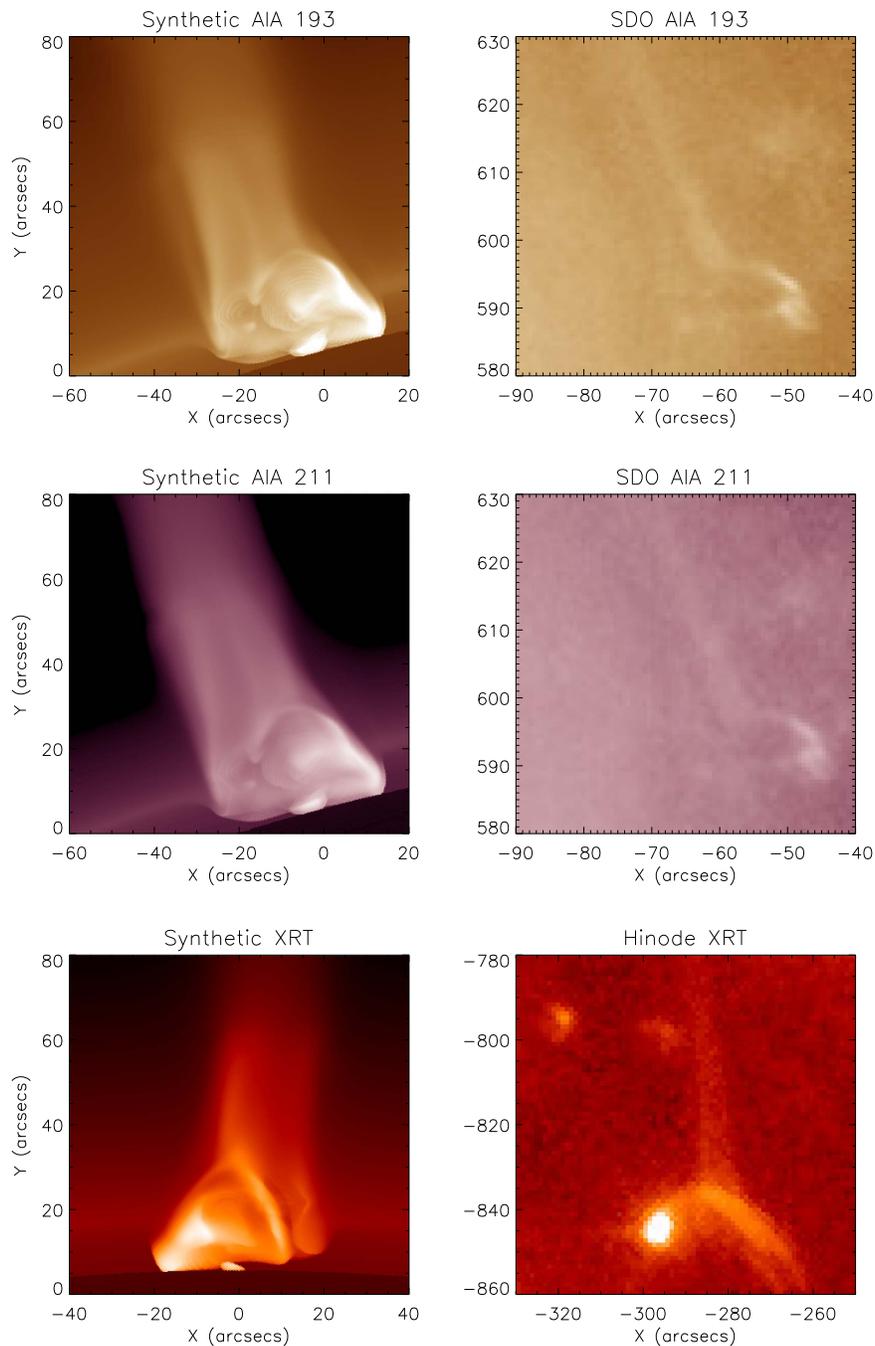
**Figure 12.** Line-of-sight synthetic images of the simulated polar jet (left panels) compared to EUV and XRT observations (right panels) of Jet 3 (top and middle rows) and Jet 1 (bottom row). Both images within each pair are shown on the same logarithmic color scale. For further discussion, see Section 5.

wavelength 171 Å and at 19:02:17 UT at wavelength 335 Å, corresponding to plasma of about 0.6–0.8 million K and 2.5 million K, respectively. Due to the large field of view, the curvature of the solar surface and the ambient coronal plasma is visible. At both bands, the model jet creates a very similar geometry to the observations, especially considering the size of the dome and the jet's tail. In the bottom row on the left, we show a close-up of the jet model at $t = 2\,\mathrm{h}\,29\,\mathrm{m}$ compared to the observation at 19:02:11 UT at wavelength 131 Å. The size of the jet is similar to the AIA image on the right, and the core brightening and the strong tail on the right side of the jet are showing the same geometric structure. This band is emitted by

both cold and hot plasma. The high noise level we see in the observation is due to low counts.

These images show that the jet model reproduces observations with very good qualitative agreement, even though the model is not tailored to any specific event. The agreement is even more remarkable when one considers that the jet-generation process—rotational motions of the chromospheric plasma to energize the magnetic field—is rather simple.

Due to the strong discontinuity in energy release, there are strong temperature gradients in the jet plasma even in the corona. The heating is concentrated in the reconnection region, and then, because the coronal heating is inhibited in the outer corona, the temperature drops relative to the initial value: in the
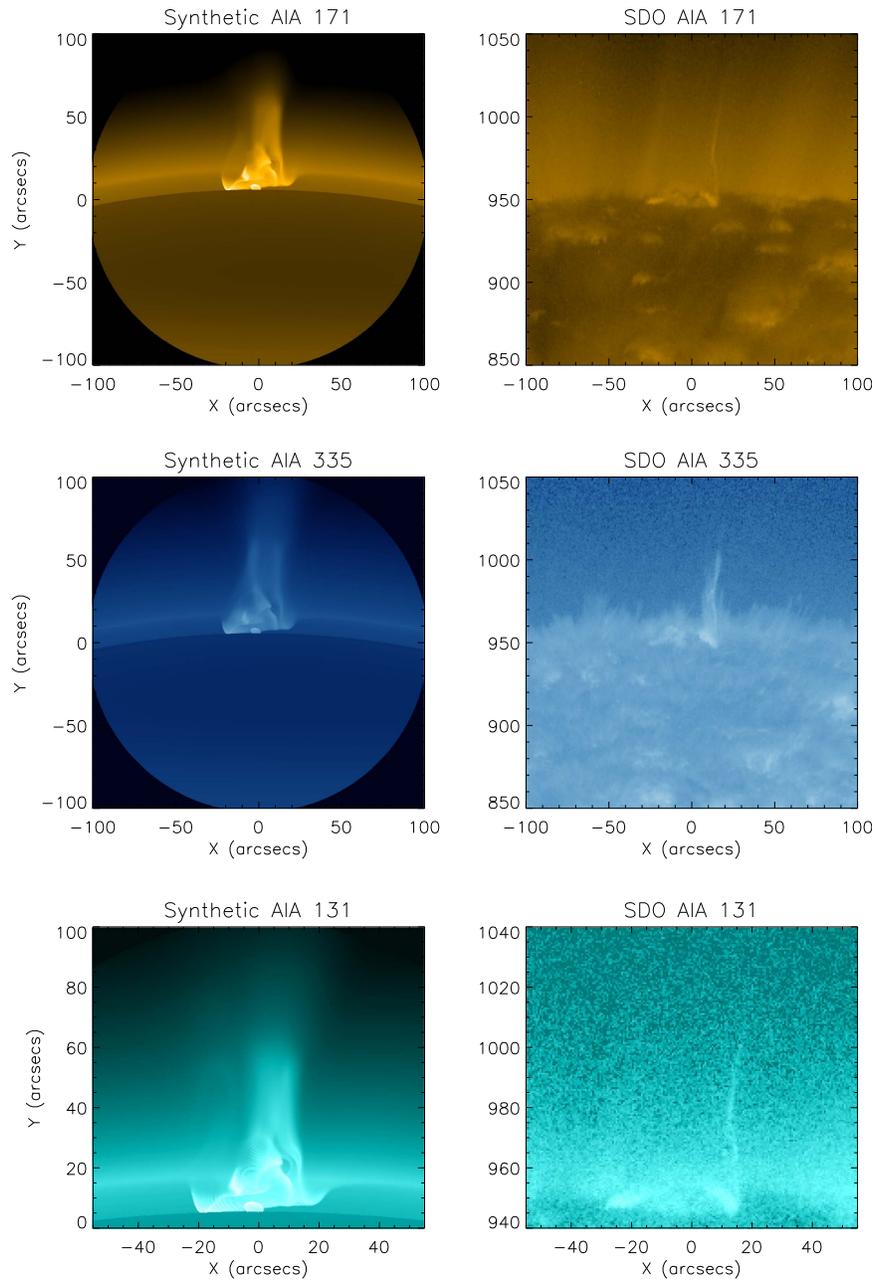
**Figure 13.** Line-of-sight synthetic and observed images in the same layout as Figure 12. The EUV observations (right panels) are of Jet 2. For further discussion see Section 5.

case of the electrons this change is already present in the low corona, and in the case of the protons, this change somewhat higher (see Figure 11). During the simulation our model shows proton temperature of the magnitude of $10^7$ K during the first bursty reconnection event, and as the periodic behavior settles, the proton temperature remains somewhat smaller, just as observed by Chifor et al. (2008a). They observed a maximum temperature about $1.3 \times 10^7$ K at the footpoint at the first, bursty jet, and decreasing temperatures later on. As discussed in Section 4.2, the electrons get heated later than protons, and to a lower temperature, due to the model implementation. This means that in the denser regions the heat gets conducted more efficiently than in low density regions, which results in brighter features in the line-of-sight images close to high-density regions. In Figures 12 and 13 we match the high-temperature observation (XRT) much better than the low-temperature ones (AIA 171, AIA 335). It might be due to the cooler ambient plasma, which contributes to low temperature filters much more than to higher temperature filters. Also, as we did not model any of these particular jets, the initial plasma conditions (magnetic field strength, electron density) are also different from the background values of the observations and produce different brightness. On the synthetic images, we observe the mixing of bright and dark areas in the jet's core, corresponding to different temperature and density regions. As shown in Figure 5, the reconnection regions where heating takes place do not necessarily coincide with the enhanced density regions.

## 6. CONCLUSIONS

We implemented a jet model based on rotational boundary motions into an advanced model for the global corona with an idealized initial magnetic field. The heating of the background corona and solar wind is produced by Alfvén-wave dissipation. Using an MHD model with separate electron and ion temperatures, we simulated two events: one located at a high magnetic latitude in an open-field region to form a polar jet, and one at a middle magnetic latitude in a closed-field region to form a loop jet. Both configurations produced an initial strong jet, and then exhibited quasi-periodic behavior in their reconnection events and the following plasma ejections. The polar jet resembles the blowout type with similarities to observations, both in physical parameters and in morphology. In our case, the jet plasma does not create a global-scale shock that would be responsible for the observed heating. Hence we conclude that the heating is due to magnetic energy release at the reconnection site.

We see large-scale perturbations caused by the jet, originating in the chromosphere and propagating out to 24 solar radii within the approximately 3 hr of simulation time. The perturbations involve Alfvén waves plus temperature and density perturbations. The magnetic untwisting loses most of its energy in the low corona (below $2.2R_\odot$), but the introduced magnetic perturbation propagates out to $24R_\odot$ within 3 hr. Following the first build-up phase, a large reconnection event is observed to be followed by oscillations of periods of about 700 s. We also see hints of another oscillation with a period of about an hour that peaks between 5000–7500 s and 8000–10,000 s. Due to the shortness of the simulation time, it is unclear whether that is a sustained phenomenon. Both the observations and our simulations are based on interchange reconnection between the twisted closed field and the open field. We find that the modeled jets produce large-scale perturbations in the solar wind, and that polar jet signatures (MHD waves) are being carried to large distances in both radial (up to 24 solar radii within 3 hr) and angular (from the pole to the equator) dimensions. Also, our polar jet caused cooling in the outer corona due to the sudden change in plasma properties (density, magnetic-field gradient, and vorticity). Cooling seems counterintuitive, as reconnection produces heating near the jet. The cooling occurs because the Alfvén wave heating is trapped by the large reflection-rate gradients, resulting in depleted energy deposition in the upper atmosphere. The polar jet signatures in the polar corona can be directly measured by several instruments on board *Solar Probe Plus*, which by reaching as far down as 9 solar radii, will be directly traveling through the jet perturbations. This study provides several observables (for example, large gradients in density and temperature) that can be directly measured by the *Solar Probe Plus* instruments.

Many questions are left open to be addressed in follow-up work. First, as mentioned in Section 1, Shimojo et al. (2007) observed that some jets cause loop brightening at the other end of the loop along closed magnetic field lines. Second, to understand the connection between the periodicity of plasma rotation and reconnection events, a parameter study would be necessary; this will also be carried out in the future. Third, the introduced numerical resistivity may have a significant effect on the amount of twist being stored between the reconnection events. We are going to address this question in our follow-up paper, in which we will use the already available fifth-order

scheme implemented by Chen et al. (2016). Finally, our results suggest that jets do not contribute significantly to the solar wind, but are important contributors to plasma waves in the corona. As Liu et al. (2015) proposed, jets might trigger larger events, for example CMEs. In that case, jets play important roles even in forming space weather. This is an interesting scenario that we will explore in a future study.

## REFERENCES

Adams, M., Sterling, A. C., Moore, R. L., & Gary, G. A. 2014, ApJ, 783, 11
Antiochos, S. K. 1990, MmSAI, 61, 369
Antiochos, S. K. 1996, in ASP Conf. Ser. 95, Solar Drivers of the Interplanetary and Terrestrial Disturbances, ed. K. S. Balasubramaniam, S. L. Keil, & R. N. Smartt (San Francisco, CA: ASP), 1
Bohlin, J. D., Vogel, S. N., Purcell, J. D., et al. 1975, ApJL, 197, L133
Brooks, D. H., & Warren, H. P. 2012, ApJL, 760, L5
Canfield, R. C., Reardon, K. P., Leka, K. D., et al. 1996, ApJ, 464, 1016
Chandran, B. D. G., Dennis, T. J., Quataert, E., & Bale, S. D. 2011, ApJ, 743, 197
Chandrashekhar, K., Morton, R. J., Banerjee, D., & Gupta, G. R. 2014, A&A, 562, A98
Chen, H.-D., Zhang, J., & Ma, S.-L. 2012, RAA, 12, 573
Chen, Y., Tóth, G., & Gombosi, T. I. 2016, JCoPh, 305, 604
Chifor, C., Isobe, H., Mason, H. E., et al. 2008a, A&A, 491, 279
Chifor, C., Young, P. R., Isobe, H., et al. 2008b, A&A, 481, L57
Cirtain, J. W., Golub, L., Lundquist, L., et al. 2007, Sci, 318, 1580
Corti, G., Poletto, G., Suess, S. T., Moore, R. L., & Sterling, A. C. 2007, ApJ, 659, 1702
Cranmer, S. R., & Woolsey, L. N. 2015, ApJ, 812, 71
Culhane, L., Harra, L. K., Baker, D., et al. 2007, PASJ, 59, 751
Doschek, G. A., Landi, E., Warren, H. P., & Harra, L. K. 2010, ApJ, 710, 1806
Fang, F., Fan, Y., & McIntosh, S. W. 2014, ApJL, 789, L19
Hollweg, J. V. 1978, RvGSP, 16, 689
Kamio, S., Hara, H., Watanabe, T., et al. 2007, PASJ, 59, 757
Karpen, J. T., DeVore, C. R., Antiochos, S. K., & Pariat, E. 2016, ApJ, in press (arXiv:1606.09201)
Kim, Y.-H., Moon, Y.-J., Park, Y.-D., et al. 2007, PASJ, 59, 763
Landi, E., Young, P. R., Dere, K. P., Del Zanna, G., & Mason, H. E. 2013, ApJ, 763, 86
Li, X., Morgan, H., Leonard, D., & Jeska, L. 2012, ApJL, 752, L22
Lionello, R., Linker, J. A., & Mikić, Z. 2009, ApJ, 690, 902
Liu, J., Wang, Y., Shen, C., et al. 2015, ApJ, 813, 115
Madjarska, M. S. 2011, A&A, 526, A19
Madjarska, M. S., Doyle, J. G., Innes, D. E., & Curdt, W. 2007, ApJL, 670, L57
Moore, R. L., Cirtain, J. W., Sterling, A. C., & Falconer, D. A. 2010, ApJ, 720, 757
Moore, R. L., Sterling, A. C., & Falconer, D. A. 2015, ApJ, 806, 11

Moore, R. L., Sterling, A. C., Falconer, D. A., & Robe, D. 2013, ApJ, 769, 134
Moreno-Insertis, F., & Galsgaard, K. 2013, ApJ, 771, 20
Moschou, S. P., Tsinganos, K., Vourlidas, A., & Archontis, V. 2013, SoPh, 284, 427
Nishizuka, N., Nakamura, T., Kawate, T., Singh, K. A. P., & Shibata, K. 2011, ApJ, 731, 43
Nishizuka, N., Shimizu, M., Nakamura, T., et al. 2008, ApJL, 683, L83
Okamoto, T. J., Tsuneta, S., & Berger, T. E. 2010, ApJ, 719, 583
Panasenco, O., Martin, S. F., & Velli, M. 2014, SoPh, 289, 603
Paraschiv, A. R., Bemporad, A., & Sterling, A. C. 2015, A&A, 579, A96
Pariat, E., Antiochos, S. K., & DeVore, C. R. 2009, ApJ, 691, 61
Pariat, E., Antiochos, S. K., & DeVore, C. R. 2010, ApJ, 714, 1762
Pariat, E., Dalmasse, K., DeVore, C. R., Antiochos, S. K., & Karpen, J. T. 2015, A&A, 573, A130
Patsourakos, S., Pariat, E., Vourlidas, A., Antiochos, S. K., & Wuelser, J. P. 2008, ApJL, 680, L73
Poletto, G., Sterling, A. C., Pucci, S., & Romoli, M. 2014, in Nature of Prominences and their Role in Space Weather, Proc. IAU Symp. 300, ed. B. Schmieder, J.-M. Malherbe, & S. T. Wu (Cambridge: Cambridge Univ. Press), 239
Powell, K. G. 1994, ICASE Report No. 94-24 (NASA Langley Research Center), http://www.icase.edu/library/reports/rdp/1994.html#94-24
Powell, K. G., Roe, P. L., Linde, T. J., Gombosi, T. I., & De Zeeuw, D. L. 1999, JCoPh, 154, 284
Pucci, S., Poletto, G., Sterling, A. C., & Romoli, M. 2012, ApJL, 745, L31
Pucci, S., Poletto, G., Sterling, A. C., & Romoli, M. 2013, ApJ, 776, 16

Savcheva, A., Cirtain, J., Deluca, E. E., et al. 2007, PASJ, 59, 771
Shen, Y., Liu, Y., Su, J., & Ibrahim, A. 2011, ApJL, 735, L43
Shibata, K. 1982, SoPh, 81, 9
Shibata, K., Ishido, Y., Acton, L. W., et al. 1992, PASJ, 44, L173
Shibata, K., Nakamura, T., Matsumoto, T., et al. 2007, Sci, 318, 1591
Shibata, K., Nitta, N., Strong, K. T., et al. 1994, ApJL, 431, L51
Shimojo, M., Hashimoto, S., Shibata, K., et al. 1996, PASJ, 48, 123
Shimojo, M., Narukage, N., Kano, R., et al. 2007, PASJ, 59, 745
Singh, K. A. P., Isobe, H., Nishizuka, N., Nishida, K., & Shibata, K. 2012, ApJ, 759, 33
Sokolov, I. V., van der Holst, B., Oran, R., et al. 2013, ApJ, 764, 23
Srivastava, A. K., & Murawski, K. 2011, A&A, 534, A62
Sterling, A. C., Harra, L. K., & Moore, R. L. 2010, ApJ, 722, 1644
Sterling, A. C., Moore, R. L., Falconer, D. A., & Adams, M. 2015, Natur, 523, 437
Sterling, A. C., Shibata, K., & Mariska, J. T. 1993, ApJ, 407, 778
Sterling, A. C., Shibata, K., & Mariska, J. T. 1994, SSRv, 70, 77
Tóth, G., van der Holst, B., Sokolov, I. V., et al. 2012, JCoPh, 231, 870
van der Holst, B., Sokolov, I. V., Meng, X., et al. 2014, ApJ, 782, 81
Wang, Y.-M., Sheeley, N. R., Jr., Socker, D. G., et al. 1998, ApJ, 508, 899
Yang, L., He, J., Peter, H., et al. 2013, ApJ, 777, 16
Yokoyama, T., & Shibata, K. 1995, Natur, 375, 42
Yokoyama, T., & Shibata, K. 1996, PASJ, 48, 353
Yokoyama, T., & Shibata, K. 1999, in The Solar Wind Nine Conf., AIP Conf. Proc. 471, ed. S. T. Suess, G. A. Gary, & S. F. Nerney (Melville, NY: AIP), 61